Mechanisms of lithospheric extension at mid-ocean ridges

Jian Lin* and E. M. Parmentier
Department of Geological Sciences, Brown University, Providence, RI 02912, USA

SUMMARY

We examine the extensional deformation of oceanic plates at mid-ocean ridges, especially within an axial yield zone where pervasive faulting occurs. Thermal models of ridges are developed which include the effects of lithospheric thickening on the mantle flow, the heat of magmatic crustal accretion at the ridge axis, and the hydrothermal cooling due to seawater circulation in the crust. When hydrothermal circulation occurs, the brittle lithospheric plate at slow-spreading ridges could be as thick as 8–9 km, thicker than the crust; while the plate at fast-spreading ridges is only 1–2 km. For a typical slow-spreading ridge, several kilometres of plate thickening are expected within a distance of 15 km from the ridge axis.

When subjected to the extensional force due to horizontal stretching, shear failure by normal faulting will occur pervasively in an axial zone, where the lithospheric plate is the thinnest. Adopting perfectly plastic rheology as a continuum description of deformation on the distributed faults, we obtain approximate solutions for the stress distribution in the yield zone. Within this yield zone, sea-floor topography increases significantly away from the ridge axis so that the resulting gravity sliding force balances the differential horizontal extensional force due to the thickening of the lithospheric plate. Basal stresses induced by the viscously deforming asthenosphere could significantly influence the stresses inside the lithospheric plate only if the mantle viscosity beneath the ridge is on the order of 10^{20} Pa s, significantly higher than generally accepted values of 10^{18} Pa s. Model calculations reveal that although the sea-floor topography at the Mid-Atlantic Ridge at 13–15 °N is regionally compensated, it is locally supported by stresses in the lithospheric plate. The deviation of the lithospheric plate from its thermal isostatic equilibrium position can be explained by necking due to plastic stretching in the axial yield zone and elastic deflection of strong plates outside the yield zone. The best fit models require the yield zones to have a half width of 10–15 km.

We find systematic variations in the gravity and topography of the East Pacific Rise, which indicate strong influence of plate spreading rate on the ridge thermal and mechanical structure. At the 16–17 °N area, where the half-spreading rate is 4.3 cm yr^{-1}, a prominent axial topographic high and an axial mantle Bouguer gravity low exist, implying a crustal or sub-crustal low density body. The gravity low disappears at the 20–21 °N area, where the half-spreading rate is 3.6 cm yr^{-1}. As the plate spreading rate decreases from 4.3 cm yr^{-1} at the 16–17 °N area to 2.7 cm yr^{-1} at the 22–23 °N area, axial ridge topography changes from higher than the thermal isostatic equilibrium position to lower than the isostatic position. The low axial topography at the 22–23 °N area can be explained by the existence of a low amplitude median valley.

Key words: spreading centre, thermal structure, plasticity, lithosphere, East Pacific Rise, Mid-Atlantic Ridge

1 INTRODUCTION

It is well known that the axial topography of slow- and fast-spreading mid-ocean ridges (MOR) is characteristically different. The axis of a fast-spreading mid-ocean ridge is characterized by a topographic high and a short wavelength positive free air gravity anomaly (*cf.* Lewis 1981, 1982;

---

* Now at: Department of Geology and Geophysics, Woods Hole Oceanographic Institution, Woods Hole, MA 02543, USA.

Madson, Forsyth & Detrick 1984). A slow-spreading ridge can be characterized by a central topographic depression flanked on both sides by a high and a large negative free-air gravity anomaly (Cochran 1979; Collette, Verhoef & de Mulder 1980). Madson *et al.* (1984) and Kuo, Forsyth & Parmentier (1986) demonstrated that a concentrated low density source is required at the ridge axis to explain the axial topographic high at the East Pacific Rise (EPR) south of 12 °N. The typical free air anomaly profile across a slow

spreading ridge is, on the other hand, well explained by a model in which there is no compensation for short wavelength topography but compensation of the ridge as a whole as predicted by a simple thermal model (Parmentier & Forsyth 1985).

To a large extent, the topography and gravity of a mid-ocean ridge depend on the ridge thermal structure. A number of ridge thermal models have been presented in which the thermal structure is determined for a prescribed velocity field (Sleep 1969, 1975; Kuznir 1980; Reid & Jackson 1981; Morton & Sleep 1985; Phipps Morgan, Parmentier & Lin 1987). Phipps Morgan *et al.* (1987) considered both the heat of magmatic crustal accretion on the ridge axis and the upwelling of mantle flow beneath the axis which are only partially included in earlier models. However, since the crustal and mantle velocities were prescribed *a priori* in these models, the effects of lithospheric thickening on the mantle velocity field were not considered. The lithosphere is defined as the mechanically strong boundary layer that overlies weak, ductile astheno-sphere. As the lithospheric plate moves away from a ridge axis and becomes thicker than the crust, a top layer of mantle becomes a part of the lithosphere and therefore moves at the same speed as the crust. In this study, we will examine the thermal structure of an oceanic lithosphere by simultaneously determining the steady-state mantle tem-perature and velocity. A numerical technique involving both finite difference and boundary element methods will be employed. We will also examine the effects of crustal hydrothermal cooling on the ridge thermal structure.

Although the mechanical structure of mid-ocean ridges depends greatly on ridge thermal structure, it is also affected strongly by crustal processes such as fissuring and faulting. A variety of observations at slow-spreading ridges suggest that the brittle lithospheric plate is extensively faulted in the median valley, and the median valley itself is formed by normal faulting along planes dipping toward the valley axis (Macdonald & Luyendyk 1977). Extensive fissures and surface faults have been discovered on the seafloor by the detailed seafloor morphology surveys of the Mid-Atlantic Ridge (MAR) at the FAMOUS area (e.g. Macdonald 1977; Macdonald & Luyendyk 1977; Crane & Ballard 1981) and the MARK area (Detrick *et al.* 1988). Global investigations of the source parameters of large earthquakes on slow-spreading ridges (Huang *et al.* 1986; Jemsek *et al.* 1986; Huang & Solomon 1987) reveal that the epicentres of such earthquakes occur in the median valley inner floor. The fault plane solutions of the earthquakes are consistent with high-angle normal faulting. A study in the MARK area (Toomey *et al.* 1985) shows that seismicity at the ridge axis extends to depths of 7–9 km and that microearthquakes occur beneath both the inner valley and the flanking mountains. Observations of the sedimentation in the MARK area suggest that fissures and faults are active in the median valley and cease to be active beyong the flanking mountains (Detrick *et al.* 1988; L. Kong, private com-munication).

Several previous models have been proposed to explain the axial median valley and flanking mountains characteris-tic of slow spreading mid-ocean ridges. Sleep (1969) and Lachenbruch (1973, 1976) attributed the axial valley to the pressure loss associated with the vertical viscous flow of

asthenosphere in a narrow conduit beneath the ridge axis. However, as pointed out by Phipps Morgan *et al.* (1987), the temperature field associated with flow in a narrow conduit does not correspond to the shape of the narrow conduit, but instead has the form of a thermal boundary layer, with nearly horizontal isotherms, that thickens gradually with distance from the ridge axis. Thus if a steady-state ridge axis conduit does exist, the strength difference between asthenosphere and conduit walls must be attributed to a significant strength reduction due to the presence of partial melt in the rising asthenosphere, by an increased strength of depleted residual mantle forming the conduit walls, or by some other, non-thermally controlled mechanism. Tapponier & Francheteau (1976) have con-sidered a steady-state necking model that quantitatively treats the regional compensation of a ridge axial depression using elastic flexure. Their model produces flanking mountains but does not predict adequate amplitude of the axial depression. Furthermore, elastic flexure can not describe the deformation of the brittle plate by dominant normal faulting in the median valley.

The numerical models of Sleep & Rosendahl (1979) were the first to include the effects of a viscous-plastic plate and quantitatively predict the formation of an axial valley. The rheological differences of the lithosphere, asthenosphere and magma chamber were characterized by changes in viscosity. Constant stresses were assumed, above which the lithospheric material deforms plastically. However, the complexity of these models does not give a simple understanding of the mechanism(s) causing the axial valley.

The observation of sea-floor morphology and the consideration of ridge thermal structure and the basalt and olivine rheology suggest the following simplified MOR mechanical model: in the asthenosphere, mantle deforms in a ductile manner due to high temperature; in the lithosphere, crust and mantle deform in a brittle manner. There are two mechanically distinctive regions in the lithosphere: within a certain distance from the ridge axis, the lithosphere deforms by extensive fissuring and normal faulting, producing a median valley; outside of which sea-floor topography is created by the elastic flexure of the thicker and stronger plates. In this study, a perfectly plastic material is adopted as a continuum description of deformation on the distributed faults in the axial yield zone. Viscously deforming asthenosphere exerts basal stresses on the brittle lithospheric plate; the plastic and elastic regions in the lithospheric plate are coupled through the stress and displacement continuity. We will analyse the stress distribution within the axial yield zone and examine how the deformation within it is controlled by the variation in: (i) brittle lithospheric plate thickness, (ii) seafloor topography, and (iii) basal stresses induced by viscously deforming asthenosphere. Model studies will be carried out to analyse the steady-state stretching of the lithospheric plates at segments of the Mid-Atlantic Ridge.

The existence of a magma chamber at a fast spreading ridge is consistent with both seismic reflection (Detrick *et al.* 1987) and gravity studies (Madsen *et al.* 1984; Kuo *et al.* 1986). So far there has been no conclusive evidence suggesting the existence of a steady-state magma chamber at slow spreading ridges. Based on our thermal and mechanical model, we will examine gravity and topography at three

segments of the EPR with moderately fast-spreading rates to address the question of whether the existence of a concentrated low density body is required at these ridges.

2 THERMAL MODEL OF MID-OCEAN RIDGES

The mechanical strength of oceanic lithosphere depends greatly on its thermal structure. A number of ridge thermal models have been presented in which the crustal and mantle velocity fields were determined *a priori* (e.g. Sleep 1969, 1975; Kuznir 1980; Reid & Jackson 1981; Morton & Sleep 1985). The most complete model (Phipps Morgan *et al.* 1987) considers both the heat of magmatic crustal accretion and upwelling mantle flow beneath the ridge axis. Even in this model, however, the effects of lithospheric thickening on the mantle velocity field have not been included. As an oceanic plate moves away from the ridge axis, cooling continues down into the mantle. As a result, a top layer of the mantle becomes part of the lithosphere and therefore moves at the same speed as the crust. Since the lithospheric plate thickness is determined by the ridge thermal structure which in turn is affected by the changes in the mantle velocity due to the lithospheric thickening, a numerical scheme is needed to compute self-consistent sets of temperature and velocity fields.

We start by assuming that the crust, which is originally emplaced at the ridge axis, moves horizontally at a constant rate, and that the underlying mantle deforms as an induced flow in a viscous halfspace with uniform viscosity. A constant crustal thickness of 6 km and a deep mantle temperature of 1400 °C are assumed. The temperature of the magmatically emplaced material in the crust at the ridge axis is adjusted to represent the heat of fusion of molten basalt (320 kJ kg^{-1}).

The corresponding thermal structure is calculated using finite difference approximations with the distribution of grid points shown in Fig. 1(a). The finite-difference approxima-

tions employed in this study are described by Phipps Morgan *et al.* (1987). From this starting thermal structure, we obtain a first iteration of the lithospheric plate thickness as given by the 700 °C isotherm (Wiens & Stein 1984; Bergman & Solomon 1984). An isotherm is used here to define the boundary between the lithosphere and asthenosphere, since the transition from the brittle regime to the ductile regime is relatively sharp. As expected, beyond a certain distance from the ridge axis, the thermal conduction causes the lithospheric plate to become thicker than the crust. Since a top layer of mantle has become part of the lithosphere, our originally assumed mantle velocity field needs to be modified. This requires the mantle velocity in the asthenosphere to be calculated.

In general, the bottom of the lithospheric plate is a smooth curved boundary. If a finite difference approximation is employed to calculate the asthenospheric velocity, this smooth boundary has to be inaccurately approximated by steps. Instead, we calculate mantle velocity using a boundary element method (BEM) analogous to that described by Crouch & Starfield (1983) and Phipps Morgan *et al.* (1987). The BEM is ideal for obtaining solutions for piecewise continuous regions with irregular boundaries. Boundary elements (short segments in Fig. 1b) are placed along the top boundary (bottom of the lithospheric plate) and the other three straight boundaries. Stresses at the element midpoints along the lithosphere–asthenosphere boundary are expected to be accurate to better than 5 per cent for all the lithosphere thickness distributions. The velocity field is calculated with boundary conditions as described by Phipps Morgan *et al.* (1987).

Based on the mantle velocity obtained by the BEM, a new iteration of thermal structure is constructed next. A newly inferred lithospheric plate thickness is then used to obtain the next iteration of mantle velocity. The iterations proceed until the calculated lithospheric thicknesses of successive iterations agree. The calculated steady-state thermal structures and velocity fields are shown in Fig. 2(a)
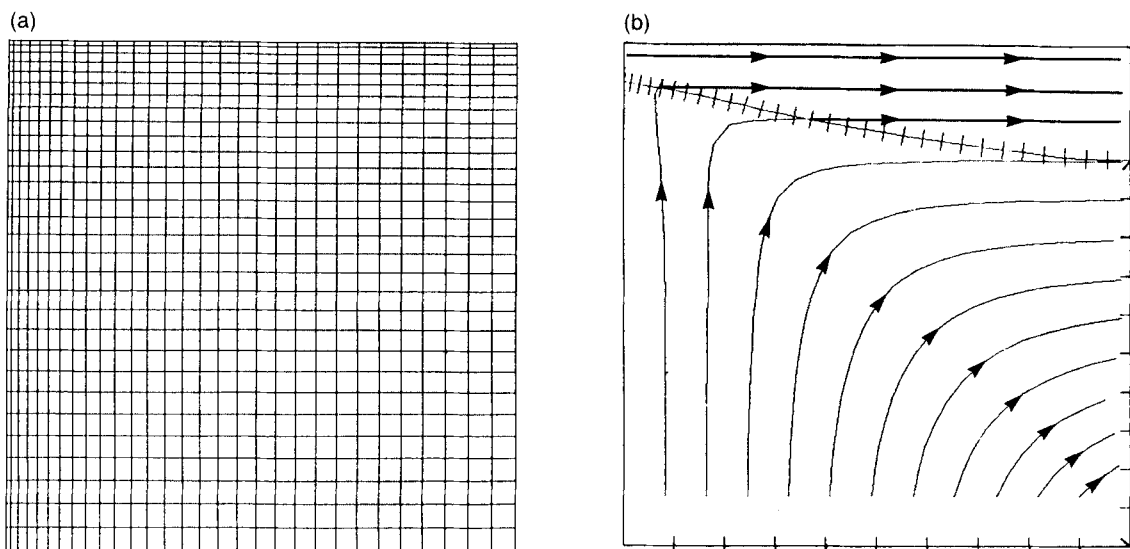

Figure 1. (a) Finite difference grids used in the calculations of ridge thermal structure. (b) Boundary elements (confined by the short bars) used in the calculations of mantle velocity field. Flow direction is indicated by the arrows.
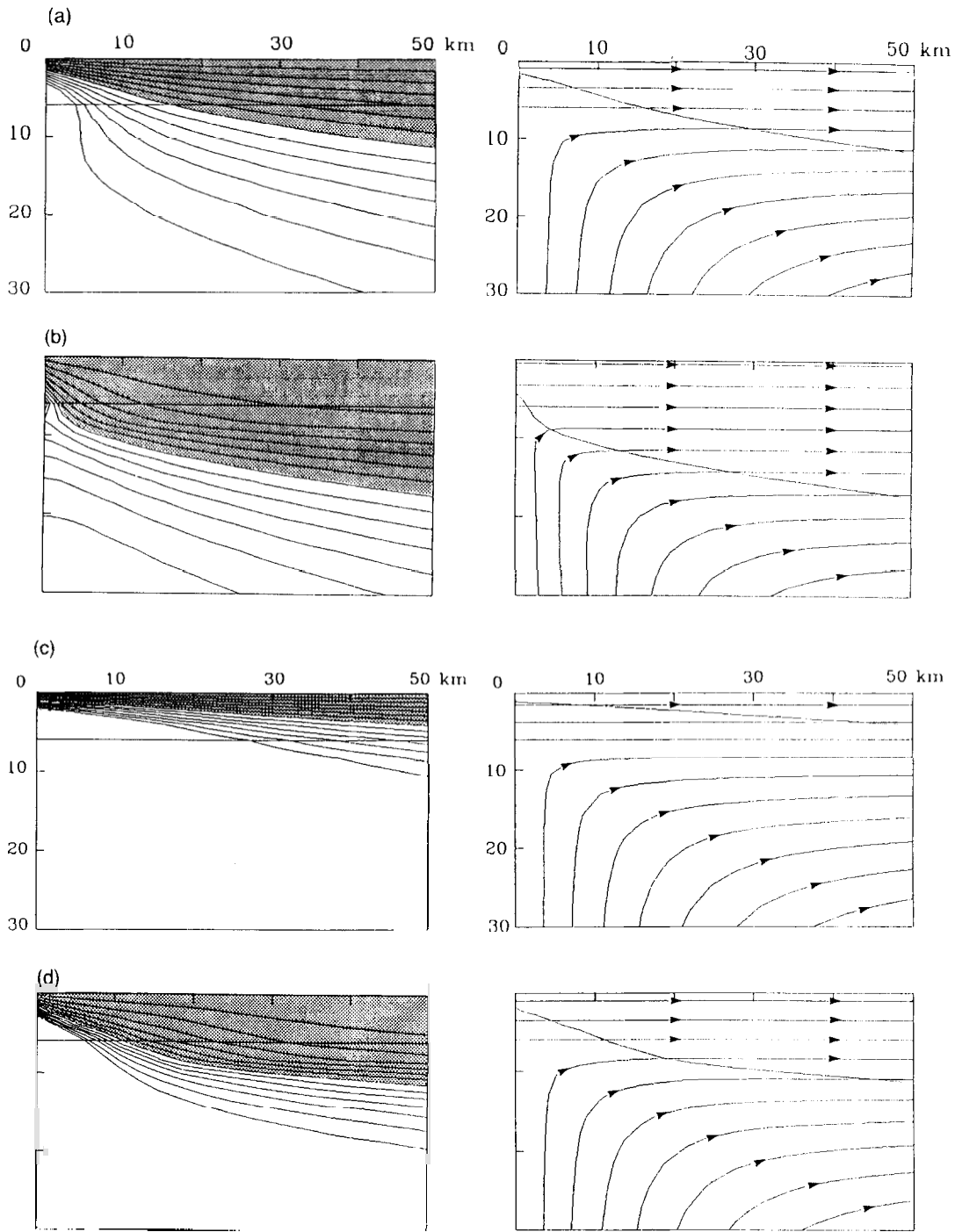
Figure 2. Thermal structure (left) and velocity field (right) for mid-ocean ridges. On the left diagrams, isotherms are shown with temperature increments of 100 °C. On the right diagrams, arrows indicate flow direction. (a) $Nu = 0$, half-spreading rate is $1\,\text{cm}\,\text{yr}^{-1}$. (b) $Nu = 6$, half-spreading rate is $1\,\text{cm}\,\text{yr}^{-1}$. (c) $Nu = 0$, half-spreading rate is $5\,\text{cm}\,\text{yr}^{-1}$. (d) $Nu = 10$, half-spreading rate is $5\,\text{cm}\,\text{yr}^{-1}$.

and (c) for plates with half-spreading rates of 1 and $5\,\text{cm}\,\text{yr}^{-1}$, respectively.

According to the thermal model of Fig. 2(a), which only takes into account of the heat conduction through seafloor, the axial lithospheric plate thickness is only a small fraction of the crustal thickness. However, recent study of the microearthquake activity at the Mid-Atlantic Ridge at 23 °N reveals that seismicity at the ridge axis extends to depths of 7–9 km beneath the seafloor and that microearthquakes

occur beneath the median valley and the flanking mountains (Toomey *et al.* 1985). This finding suggests that the brittle plate thickness at this segment of the slow spreading ridge is at least 7–9 km, much thicker than that predicted by the simple thermal model (Fig. 2a). Therefore, other mechanisms which can contribute to the plate thickening at the ridge axis need to be considered.

Hydrothermal convection of seawater through permeable oceanic crust is widely recognized as an important
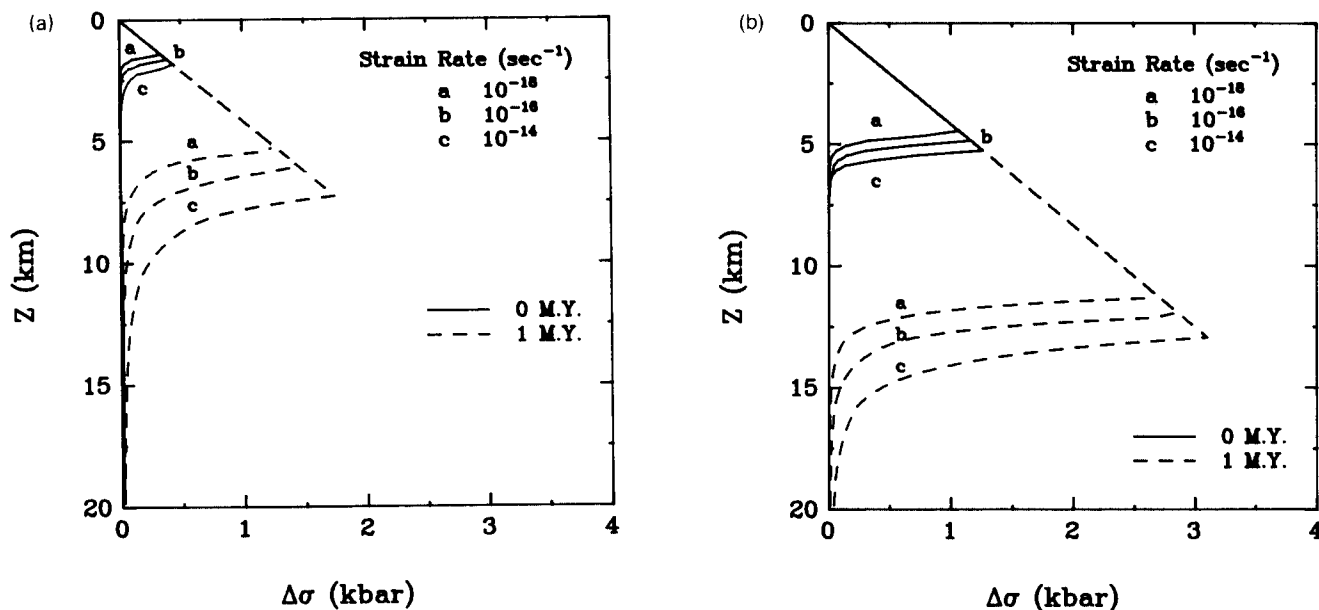
Figure 3. Extensional strength of an oceanic lithospheric plate with zero age (the solid lines) and an age of 1 Myr (the dashed lines). The brittle and ductile strength are shown by the straight and curved lines, respectively. (a) Corresponding to the thermal structure of Fig. 2(a) (without the crustal hydrothermal cooling). (b) Corresponding to the thermal structure of Fig. 2(b) (with the crustal hydrothermal cooling).

mechanism of heat transfer, particularly in young oceanic crust (Lister 1983). Seafloor hydrothermal vents have been observed at numerous locations along both the EPR (e.g. Spiess *et al.* 1980) and the MAR (Rona 1985; ODP Leg 106 Scientific Party 1986). To examine the effects of hydrothermal cooling in a simple way, heat transfer due to seawater circulation in the crust is represented as an increased thermal conductivity (Phipps Morgan *et al.* 1987). The ordinary thermal conductivity is enhanced by a factor Nu, the Nusselt number for hydrothermal convection in a permeable layer. Rock at a temperature greater than 400 °C or at depth greater than 6 km is assumed to be impermeable because it cannot support open fractures. The thermal model in Fig. 2(b), with the same spreading rate as in Fig. 2(a), is calculated for Nu = 6. With the additional heat loss due to hydrothermal cooling in the crust, the lithospheric plate (the shaded area in Fig. 2b) is much thicker at the ridge axis.

The effect of the hydrothermal cooling on ridge thermal structure can be demonstrated more clearly by a comparison of the extensional strength of the lithospheric plates (Fig. 3). The extensional strength of a lithospheric plate measures the maximum differential stress that can be supported by the plate. Based on the brittle and ductile rheology for olivine as given by Brace & Kohlstedt (1980), we calculate the strength of lithospheric plates with the thermal structures of Fig. 2(a) and (b). It is observed that the overall strength of an oceanic plate is enhanced greatly due to the hydrothermal cooling. It is also observed that the brittle strength (limited by the straight lines in Fig. 3) is much greater than the ductile strength (limited by the curved lines) and that the brittle part of the plate accounts for the vast majority of the strength of the lithosphere.

Calculations reveal that with a Nu number equal to or less than 7, the lithospheric plate at a slow-spreading ridge axis remains thinner than the crust, and the continuous crustal accretion accommodates steady-state plate spreading. When

the Nu number is greater than 7, great heat conduction moves the boundary between the lithosphere and asthenosphere at the ridge axis down into the mantle. In this case, continuous crustal emplacement alone is not sufficient to maintain the steady-state plate spreading at the ridge axis; the part of the mantle that is within the brittle lithospheric plate should stretch mechanically.

The observed 7–9 km depth of seismicity at the MAR 23 °N may not represent the steady-state lithosphere thickness at the MAR. Petrological and geophysical evidence suggest that the spreading process at mid-ocean ridges is not continuous, but rather episodic; this episodicity depends strongly on the plate spreading rate and eruption volume. For example, the estimated eruption interval between individual basaltic flows at the Mid-Atlantic Ridge is 5000–10 000 years (Bryan & Moore 1977; Atwater 1979; Stakes *et al.* 1984). On the other hand, a slightly different analysis yields an eruption interval of approximately 50 yr for the fast spreading EPR (Lonsdale 1977; Schouten & Denham 1979). When the plate spreading rate is slow, even within a ridge segment bounded by two major fracture zones, great variations in geological character of the median valley may occur. For example, recent studies (Karson *et al.*, 1987; Detrick *et al.* 1988) suggest that the northern segment of the ridge at the MARK area has experienced extreme stretching and volcanic construction is dominant at the present time. Here the crust has suffered great tectonic extension and robust magmatism has led to an extremely large constructional volcanic ridge. In contrast, the southern portion of the ridge at the MARK area represents a stage when stretching is dominant. Here volcanism is expressed by small volcanic cones, and no youthful neovolcanic zone exists. The seismic study of Toomey *et al.* (1985) was carried out within this portion of the MAR ridge.

Let us assume that the steady-state lithospheric plate thickness at the axis of the MAR is about 6 km when the ridge begins its stretching-dominant stage. With a normal
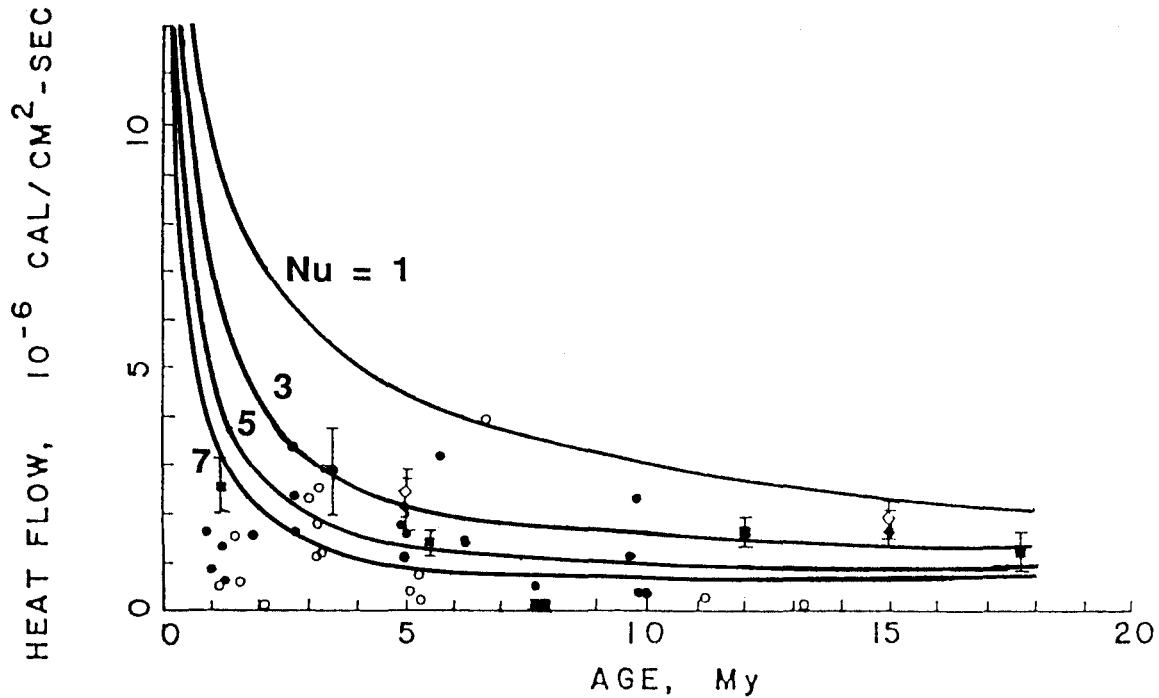
Figure 4. Predicted versus observed heat flow at slow spreading mid-ocean ridges. Observed data were originally compiled by Wolery & Sleep (1976): (●) Reykjanes Ridge (Talwani, Windish & Longseth 1971); (○) Mid-Atlantic Ridge near 45 °N (Hyndman & Rankin 1972); (◆, ◇) Mid-Atlantic Ridge, South Atlantic (Sclater & Francheteau 1979); (■) Atlantic-Indian ocean mean (Le Pichon & Langseth 1969). Error bars indicate standard errors for points obtained by averaging a number of individual measurements. Theoretical predictions with assumed Nu numbers of 1, 3, 5 and 7 are shown by solid lines.

crustal thermal diffusivity of $10^{-6} \, m^2 \, s^{-1}$, about $10^5 \, yr$ are needed for pure heat conduction to move the bottom of the lithospheric plate down to a depth of 8 km. The additional heat loss by the seawater circulation in the crust can, however, reduce this required time substantially. If the effective thermal conductivity of the crust is enhanced by a factor of 10 due to the hydrothermal cooling, only $10^4 \, yr$ is needed to cool the lithospheric plate downward 2 km solely by heat conduction through the seafloor. This time scale is close to the lower limit of the estimated tectonic episodicity of the MAR.

We calculate heat flow by using the vertical temperature gradients given by the thermal models. The theoretically predicted heat flow with assumed Nu number of 1, 3, 5 and 7 are shown in Fig. 4 along with the heat flow data observed at the slow-spreading ridges. Sufficiently far away from the ridge axis, say beyond 5 Myr of crustal age, the average observed heat flow is best explained by a model with Nu number of 5. At seafloor very close to the ridge, the observed heat flow is, however, better explained by higher Nu numbers. The apparent increase in Nu number toward the ridge axis implies the greater importance of crustal hydrothermal cooling at ridge axis. A higher degree of cracking and faulting at the ridge axis can provide greater permeability for the hydrothermal circulation and enhance the degree of hydrothermal cooling.

Comparison of thermal structures with and without hydrothermal cooling is shown in Fig. 2(c) and (d) for a fast spreading ridge with a half spreading rate of $5 \, cm \, yr^{-1}$. Even with a Nu number as high as 10, the lithospheric plate at a fast spreading ridge remains 2–3 km thick. This

thickness is consistent with the interpretations based on the seismic refraction study of the EPR 12 °N (Detrick *et al.* 1987). A very thin plate at fast-spreading ridges is also consistent with the fact that no large earthquakes have ever been observed at the axis of fast-spreading ridges.

To estimate the sea floor topography due to thermal isostasy, we further calculate the mantle thermal buoyancy force $P(x)$ which acts on the bottom of the lithospheric plate (the solid line in Fig. 5). We calculate $P(x)$ by integrating the thermal buoyancy in each vertical column from the surface to a depth of 100 km, where horizontal temperature
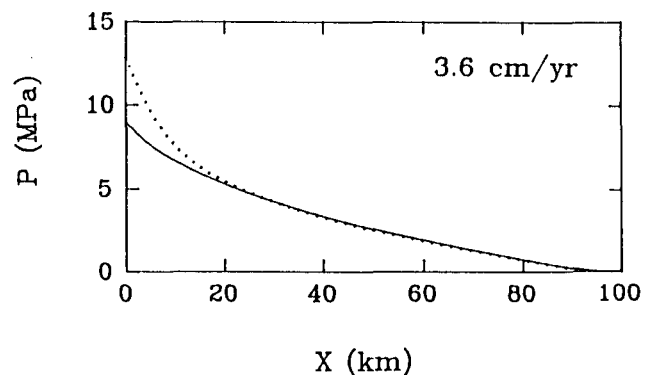

Figure 5. Predicted thermal buoyancy force due to density deficiency in the mantle. The solid line represents a case when hydrothermal cooling in the crust is not considered. The dotted line represents a case when the effective thermal conductivity of the crust is enhanced by a factor of 10 due to hydrothermal cooling.

variation is negligible. It is observed that the rate of decrease in the thermal buoyancy $P(x)$ away from the ridge axis is greater when hydrothermal convection occurs in the crust (the dashed line in Fig. 5). Its effect on the seafloor topography is, however, offset by the increase in the plate strength due to increased plate thickness. These estimations are useful for our later study of the tectonics of the East Pacific Rise.

In summary, hydrothermal cooling greatly enhances heat transfer at mid-ocean ridges and makes the lithospheric plates at slow-spreading ridges much thicker. Given the same amount of hydrothermal cooling (same Nu number), the slower the spreading rate is, the faster the plate thickens as it moves away from the ridge axis. For a typical slow-spreading ridge, several kilometres of plate thickening are expected within a distance of 15 km from the ridge axis.

Based on these results for the mid-ocean ridge thermal structure, we will further explore the mechanical structure of ridges. We are particularly concerned with the plastic rheology of the lithospheric plate, since when subjected to sufficient extensional force, shear failure is expected to occur pervasively in an axial zone at the ridge axis, where the brittle lithospheric plate is thinnest (Lin & Parmentier 1987). In the next section, we will study the brittle deformation of the lithosphere and will show that the thickening rate of the lithosphere is one of the most important factors in controlling the seafloor topography.

3 PLASTIC DEFORMATION OF THE OCEANIC PLATE AT MID-OCEAN RIDGES

Extensive fissures and normal faults significantly weaken lithospheric plates at mid-ocean ridges. Fine scale seafloor morphological studies reveal that the oceanic crust at mid-ocean ridges is highly fractured and that normal faulting accounts for the vast majority of ridge relief. At the slow-spreading MAR, normal faults with an average spacing of about 1–2 km and an average throw of 150 m occur parallel

to the spreading axis (Macdonald & Luyendyk 1977; Laughton & Searle 1979). While the fault spacing at the fast-spreading EPR is similar to that of the MAR, the average fault throw is only 20–40 m (Searle 1984; Bicknell *et al.* 1986). Although fault scarps have been found in the seafloor tens of kilometres from the ridge axis, observations of the sedimentation in the MARK area suggest that fissures and faults are active primarily in the median valley and cease to be active beyond the flanking mountains (Detrick *et al.* 1988; L. Kong, private communication). Studies at the MAR indicate that there is no significant change in fault throw beyond the crestal mountains and the spacing between faults does not decrease with distance from the ridge axis, implying that few new faults are generated outside the median valley (Laughton & Searle 1979).

The extensional strains accumulated during the stretching-dominant stage in the ridge tectonic cycle are much more easily be released by slip on the pre-existing normal faults than by elastic extension of the un-faulted parts of a plate. With a tectonic cycle length on the order of 10 000 yr, only 10 m of slip need to occur on pre-existing normal faults during the entire stretching-dominant stage of a volcanism-stretching tectonic cycle. From this consideration, the observed 150 m of average throw on the normal faults might well be the results of successive slip on the same faults during different tectonic cycles.

The mechanical model of a slow-spreading MOR, shown in Fig. 6, reflects the characteristics of the observed oceanic crust faulting and the thermal structure discussed in the last section. The 600–700° isotherm determines the transition from brittle to ductile deformation and defines the boundary between the brittle lithospheric plate and the viscously deforming asthenosphere. In the brittle plate, there are two regions: the first region (yield zone), within a distance L from the ridge axis, is characterized by extensive fissuring and normal faulting. The second area (strong plate), outside L, is characterized by motion at a constant horizontal velocity and seafloor topography that is generated by the
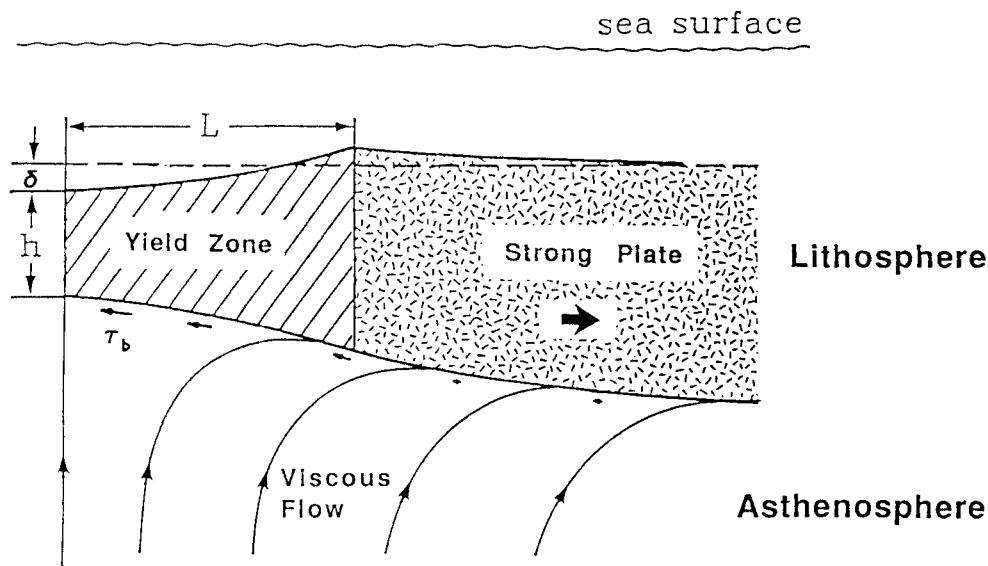

Figure 6. Mechanical model of a slow spreading mid-ocean ridge. L is the width of the axial yield zone, in which pervasive shear failure occurs. h is the thickness of the brittle lithospheric plate. δ is seafloor topography, and $\tau_b = -\sigma_s$ is the basal shear stress induced by the asthenospheric flow.

elastic flexure of the plate. In this region, the extension by faulting ceases due to the lack of sufficient extensional stress in the gradually thickening plate (Lin & Parmentier 1987).

The viscously deforming asthenosphere and the brittle lithospheric plate are related through the stress and velocity continuity. For example, viscous flow in the asthenosphere exerts basal stresses on the bottom of the plate (Fig. 6). The plastic and elastic regions are also related through the stress and displacement continuity. In the following, we will first analyse the stress distribution in the axial yield zone, and study how the deformation within it is controlled by seafloor topography, plate thickness variation, and viscous mantle flow. A model study of a slow spreading ridge will then be carried out and the results will be applied to the MAR. This model can also apply to ridges with moderately fast spreading rates, such as the EPR at 20–23 °N.

3.1 Formulation of the model

Our model for an extensively faulted plate consists of a homogeneous brittle layer of deformable noncohesive Coulomb material, which is extended by a pulling force from its ends and overlies a viscously deforming mantle (Fig. 6). Our strategy is not to model the details of deformation on individual normal faults in the yield zone; instead we are more interested in the stress distribution in the yield zone when the deformation on the distributed faults are approximated by a continuum plastic rheology. We are compelled by mathematical difficulties to disregard the elastic component of strain, since it is usually very small in comparison with the plastic component (Hill 1950). Let $d\delta/dx$ be the local slope of topographic relief and dh/dx be

the local plate thickness change. A system of local Cartesian coordinates x, z will be employed, with x horizontal and z vertical. The local height of the water overburden, measured along the direction of gravity, will be denoted by D (Fig. 7a).

For convenience we denote $\bar{\sigma}_{xx}$ as the total horizontal extensional stress and σ_{xx} as the stress in excess of the lithostatic and water overburden, namely

$$\bar{\sigma}_{xx} = -\rho g z - \rho_w g D + \sigma_{xx}. \tag{1a}$$

Similarly,

$$\bar{\sigma}_{zz} = -\rho g z - \rho_w g D + \sigma_{zz} \tag{1b}$$

$$\bar{\sigma}_{xz} = \sigma_{xz}, \tag{1c}$$

where ρ and ρ_w are the densities of the lithosphere and water, respectively, and g is the acceleration of gravity. The excess substratum stress at the bottom of the layer can be written as:

$$\bar{\sigma}_{xx}^s = -\rho g h - \rho_w g D + \sigma_{xx}^s \tag{2a}$$

$$\bar{\sigma}_{zz}^s = -\rho g h - \rho_w g D + \sigma_{zz}^s \tag{2b}$$

$$\bar{\sigma}_{xz}^s = \sigma_{xz}^s. \tag{2c}$$

Denoting σ_n as the normal traction of the substratum (Fig. 7a) and σ_s as the basal shear stress, within a small angle approximation,
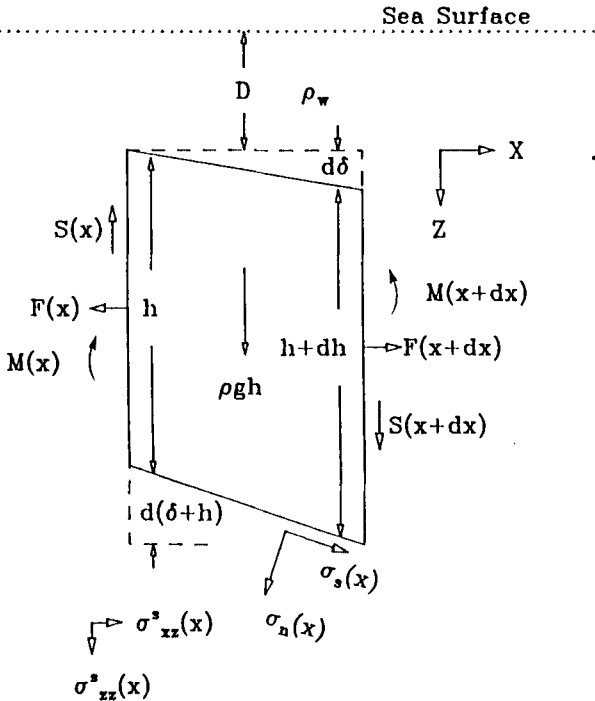
$$\sigma_n = \sigma_{zz}^s + 2\sigma_{xz}^s \, d(\delta + h)/dx \tag{3a}$$

$$\sigma_s = (\sigma_{zz}^s - \sigma_{xx}^s) \, d(\delta + h)/dx + \sigma_{xz}^s. \tag{3b}$$

In the limit of small mantle viscosity, σ_{zz}^s corresponds to the hydrostatic restoring force

$$\sigma_n = \sigma_{xx}^s = \sigma_{zz}^s = -\Delta \rho g \delta \tag{4a}$$
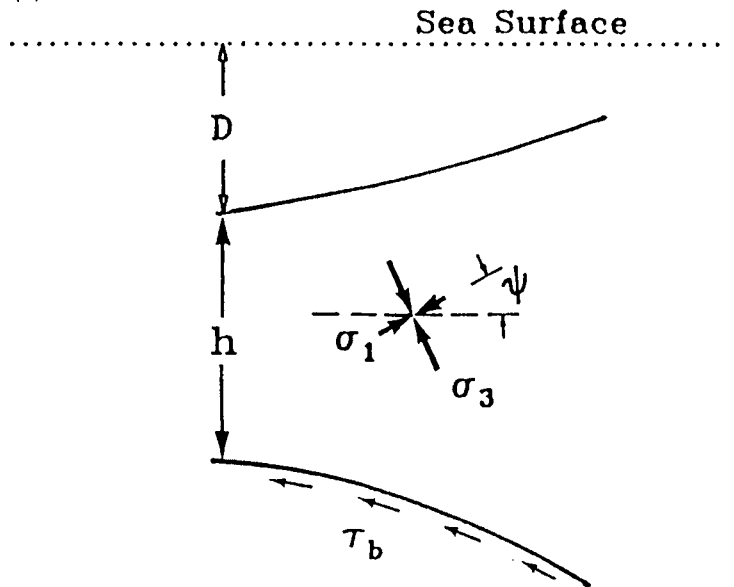
(a)

(b)

Figure 7. (a) Forces and torques in a vertical column of an oceanic lithospheric plate. Also shown are stresses in the asthenosphere (with superscript *s*). (b) ψ is the orientation of maximum extensional principal stress with respect to the horizontal.

Table 1. Notation

Variable	Meaning	Value used	Dimension
ρ_w	density of water	1.03	Mg m^{-3}
ρ	density of lithosphere	3.0	Mg m^{-3}
ρ_m	density of mantle	3.4	Mg m^{-3}
$\Delta\rho$	$=\rho_m - \rho_w$	2.37	Mg m^{-3}
g	acceleration due to gravity	9.8	ms^{-2}
U	half-spreading velocity		ms^{-1}
ΔT	deep mantle temperature	1400	$^\circ$C
α	thermal expansion coefficient	3×10^{-5}	$^\circ$C^{-1}
κ	thermal diffusivity	10^{-6}	m^{2}s^{-1}
Nu	Nusselt number of hydrothermal convection		
L	width of axial yield zone		km
x	horizontal distance		km
z	vertical distance		km
h	lithospheric plate thickness		km
h_c	constant crustal thickness	6	km
D	local height of water overburden		km
δ	topographic height		km
$\bar\sigma_{xx}$	total horizontal stress		Pa
$\bar\sigma_{zz}$	total vertical stress		Pa
$\bar\sigma_{xz}$	total shear stress		Pa
$\sigma_{xx},\sigma_{zz},\sigma_{xz}$	stresses in excess of lithostatic and water overburden		Pa
$\bar\sigma^s_{xx}$	total substratum horizontal stress		Pa
$\bar\sigma^s_{zz}$	total substratum vertical stress		Pa
$\bar\sigma^s_{xz}$	total substratum shear stress		Pa
$\sigma^s_{xx},\sigma^s_{zz},\sigma^s_{xz}$	substratum stresses in excess of lithostatic and water overburden		Pa
σ_n	normal traction of the substratum		Pa
σ_s	basal shear stress		Pa
σ_1	maximum principal stress		Pa
σ_3	minimum principal stress		Pa
P_f	pore fluid pressure		Pa
$\bar\sigma_{xx}^*$	effective horizontal stress =horizontal stress-pore pressure		Pa
$\bar\sigma_{zz}^*$	effective vertical stress		Pa
P	thermal buoyancy force		N m^{-1}
F	horizontal normal traction force in the plate		N m^{-1}
S	vertical shear force in the plate		N.m^{-1}
μ	friction coefficient on fault surface	0.6	
ϕ	$=\tan^{-1}\mu$, angle of friction	26	$^\circ$
λ	Hubbert and Rubey pore fluid pressure ratio	0.5	
η	mantle viscosity		Pa s
ψ	angle between maximum extensional principal stress and x axis		
ψ_t	value of angle ψ at top of the plate		
ψ_b	value of angle ψ at bottom of the plate		
ψ_a	depth-averaged value of ψ		

and

$$\sigma_s = \sigma^s_{xz} = 0, \tag{4b}$$

where $\Delta\rho = \rho_m - \rho_w$, ρ_m is mantle density, and δ is deflection of the plate from its isostatic equilibrium position (positive downward). Notation for variables is described in Table 1.

Let us enumerate the forces acting on the segment of unit length along strike (i.e. in and out of the page) lying between x and $x + dx$. There are four forces along the x-axis. The first is a gravity sliding force due to seafloor topography $\Delta\rho gh\, d\delta(x)/dx$. The second force is due to the basal shear stress $\sigma_s(x)$ from the viscously deforming athenosphere; it is a function of mantle viscosity and plate spreading velocity. If $F(x)$ represents the normal traction force acting across the whole layer thickness, the third force is then equal to the resultant extension produced by the normal tractions acting on the vertical faces of the column. The fourth force is the horizontal component of the traction from the substratum. Balancing forces requires in the limit $dx \to 0$ that

$$dF/dx + \sigma_s + \Delta\rho gh\, d\delta/dx - \sigma_n\, d(\delta + h)/dx = 0, \tag{5a}$$

where

$$F(x) = \int_0^{h(x)} \sigma_{xx}\, dz. \tag{5b}$$

The vertical force balance requires:

$$dS/dx + \sigma_n + \sigma_s\, d(\delta + h)/dx = 0, \tag{6a}$$

where $S(x)$ is the vertical shear force acting on the element

$$S(x) = \int_0^{h(x)} \sigma_{xz}\, dz. \tag{6b}$$

In the limit of low mantle viscosity (equation 4), equations (5a) and (6a) become

$$dF/dx + \Delta\rho gh\, d\delta/dx + \Delta\rho g\delta\, d(\delta + h)/dx = 0 \tag{5c}$$

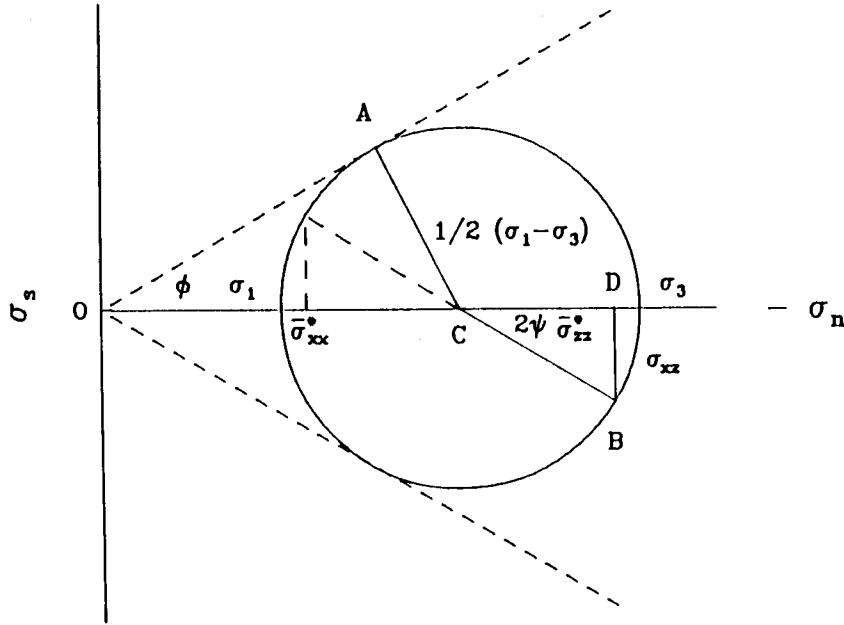$$dS/dx - \Delta\rho g\delta = 0. \tag{6c}$$

Figure 8. Mohr-diagram shows stresses in a brittle layer which is at yield throughout. ϕ is the angle of internal friction. ψ measures the direction of maximum principal stress.

Note that when seafloor topography δ is small compared to plate thickness h, the third term in equation (5c) is much less than the second term.

To determine $F(x)$ and $S(x)$, we must consider the state of stress within the plate in more detail. As was shown in the last section, the brittle strength accounts for more than 90 per cent of the overall strength of an oceanic lithospheric plate (Fig. 3). Therefore, brittle deformation is dominant in the lithospheric plate. We assume that the material within an axial zone in the brittle plate is on the verge of shear failure throughout. The observed seafloor fissures and faults and the seismic faulting are examples of shear failure.

A Mohr-circle representation of the stress at an arbitrary point in a plate at yield is shown in Fig. 8. The maximum and minimum effective stresses are denoted by σ_1 and σ_3, respectively. The local angle between the axis of maximum extensional stress and the x axis is denoted by ψ (*cf.* Fig. 7b). By inspection of triangle BCD in Fig. 8 we see that

$$\sigma_{xx} - \sigma_{zz} = \bar{\sigma}_{xx}^* - \bar{\sigma}_{zz}^* = \cos 2\psi(\sigma_1 - \sigma_3), \tag{7}$$

whereas from triangle OAC we find

$$\sigma_1 - \sigma_3 = \sin \phi(\bar{\sigma}_{xx}^* + \bar{\sigma}_{zz}^*), \tag{8}$$

where the angle ϕ is related to the frictional coefficient by $\mu = \tan \phi$, the asterisk denotes the effective stresses (stresses—pore fluid pressure). A combination of equations (7) and (8) yields

$$\sigma_{xx} - \sigma_{zz} = -2\bar{\sigma}_{zz}^*/(\csc \phi \sec \psi + 1), \tag{9}$$

where $\bar{\sigma}_{zz}^*$ is the effective vertical normal traction. This equation together with the corresponding result for the shear stress

$$\sigma_{xz} = -1/2(\sigma_{xx} - \sigma_{zz}) \tan 2\psi$$

$$= \bar{\sigma}_{zz}^*/(\csc \phi \sec \psi + 1) \tan 2\psi \tag{10}$$

completely define the state of stress within a noncohesive critically yielded layer in terms of $\bar{\sigma}_{zz}^*$ and ψ. For simplicity, we shall consider ϕ to be constant. Even in a layer with uniform properties the angle ψ will vary appreciably with x and z.

Assuming a fluid pressure which increases linearly with depth, we may write the effective vertical normal traction in the form

$$\bar{\sigma}_{zz}^* = (1 - \lambda)(\bar{\sigma}_{zz} + \rho_w gD), \tag{11}$$

where λ is the Hubbert and Rubey pore fluid pressure ratio (cf. Davis, Suppe & Dahlen 1983; Dahlen, Suppe & Davis 1984):

$$\lambda = P_f/\bar{\sigma}_{zz}, \tag{12}$$

where P_f is pore fluid pressure. The vertical normal traction should vanish at $z = 0$ and match the substratum stress at $z = h$. Introducing $q_1(x)$, $q_2(x)$, and $\cdots$ as coefficients of the higher order polynomials of z, we express $\bar{\sigma}_{zz}$ as

$$\bar{\sigma}_{zz}(x, z) = -\rho_w gD - \rho gz + \sigma_{zz}^s z/h + q_1 \rho gz(1 - z/h)$$

$$+ q_2 \rho gz(1/2 - z/h)(1 - z/h) + \cdots. \tag{13a}$$

Analytic techniques employing polynomial expansions are frequently used in the studies of elastic flexure of plates and shells (Timoshenko & Wornowsky-Krieger 1959).

In the limit of small mantle viscosity, the vertical traction should match the hydrostatic restoring pressure $\Delta\rho g\delta$ at $z = h(x)$,

$$\bar{\sigma}_{zz}(x, z) = -\rho_w gD - \rho gz - \Delta\rho g\delta z/h + q_1 \rho gz(1 - z/h)$$

$$+ q_2 \rho gz(1/2 - z/h)(1 - z/h) + \cdots. \tag{13b}$$

The angle ψ is generally a function of x and z. Introducing an x-dependent variable $\psi_a(x)$ and denoting $\psi_t(x)$ and $\psi_b(x)$ as values of ψ at top and bottom of the

layer, we have

$$\psi(x, z) = \psi_t + (\psi_b - \psi_t)z/h + 6\psi_a z/h(1 - z/h). \quad (14)$$

At the top surface of the layer, if there is the slightest cohesion, ψ must be parallel to the local topography so that $\psi_t(x) = d\delta(x)/dx$. In the small-angle approximation, $d\delta/dx$ is small and $\psi_t(x)$ is negligible. The angle ψ near the base of the layer can be found from the prescribed basal shear stress there: at $z = h(x)$,

$$(\sigma_{zz} - \sigma_{xx}) d(\delta + h)/dx + \sigma_{xz} = \sigma_s. \quad (15a)$$

Substituting equations (9) and (10) into this equation and assuming a small ψ, we get

$$2\bar{\sigma}^*_{zz}/(\csc \phi \sec \psi_b + 1)[\psi_b - d(\delta + h)/dx] = \sigma_s. \quad (15b)$$

The larger the basal shear stress, the greater the angle ψ_b. In the limit of small mantle viscosity and with the small-angle approximation, ψ_b is also negligible. When ψ_t and ψ_b are small, ψ_a represents a depth-averaged value of the angle between the maximum extensional principal stress direction and the horizontal.

We have obtained the forms of the stresses in a brittle plate which is at yield throughout (equations 9, 10, 13b and 14). We can now express $F(x)$ and $S(x)$ (equations 5b and 6b) in terms of the unknown functions $q_1(x)$, $q_2(x)$, ... and $\psi_a(x)$:

$$F(x) = (1 - \lambda)\rho g T_0 h^2 \{[1 - T_1(6/5)\psi_a^2]$$
$$+ [T_3 - 1 + T_1(6/5)\psi_a^2][-T_2(\delta/h) + (1/3)q_1 + \cdots]\} \quad (16a)$$

$$S(x) = -(1 - \lambda)\rho g T_0 h^2[1 + (4/3 - T_1)(54/35)\psi_a^2]$$
$$\times [1 + T_2(\delta/h) - (1/3)q_1 + \cdots]\psi_a, \quad (16b)$$

where

$$T_0 = \sin \phi(1 + \sin \phi) \quad (17a)$$

$$T_1 = 2/(1 + \sin \phi) \quad (17b)$$

$$T_2 = \Delta\rho/\rho \quad (17c)$$

$$T_3 = 1/[2(1 - \lambda)T_0]. \quad (17d)$$

It is noticed that q_1 and other higher order terms involving odd orders of z polynomials have contributions to F and S, while q_2 and other even order terms have no contributions to either F or S.

In the following analysis, this formulation will be used to study the steady-state topography of mid-ocean ridges. The steady-state topography is constructed based on the steady-state thermal structure discussed in the last section. We will first consider in detail the cases when basal stresses are small. Slightly simplified solutions are then obtained for the cases when mantle viscosity is finite and substrata stresses are not negligible.

3.1.1 Small basal stresses

Our goal is to derive the simplest complete model for a brittle plate which is under extension and yielding throughout. The mantle flow in the asthenosphere (as shown in Fig. 2) is controlled by the horizontal spreading velocity of the lithospheric plate. Small basal stresses at the plate bottom are expected when mantle viscosity is low. In the ideal case of a zero asthenospheric viscosity, the normal and

shear stresses acting on the bottom of the lithospheric plate are given by equation (4). Since the surface slope $d\delta/dx$ contributes to the stresses within the plate and the basal stresses also relate to δ, we can not simultaneously specify that the material in the plate be yielding and that the surface slope have a prescribed value (Chapple 1978). The surface slope $d\delta/dx$ as predicted by equation (5c) can be interpreted as that necessary for extension and yielding to occur in the plate.

We start with the simplest expression of vertical normal traction by assuming $q_1 = q_2 = \cdots = 0$. Upon substituting equations (16) into equations (5c) and (6c), we solve for two unknowns $\delta(x)$, $\psi_a(x)$. Two boundary conditions are required to determine δ and ψ_a. The first boundary condition comes from the consideration that the shear stress in the plate at the ridge axis is zero due to the symmetry of stress field about the ridge axis. It is clear from the expression of equation (16b) that requiring the shear force S to be zero is equivalent to requiring the maximum extensional principal stress to coincide with the horizontal, namely

$$\psi_a(0) = 0. \quad (18)$$

The second boundary condition is on the value of δ at the ridge axis. Without the stretching by normal faulting, the equilibrium position of a lithospheric plate is determined by flexure of the plate under the thermal buoyancy force (thermal subsidence). The deflection δ, therefore, measures the departure of the stretched plate away from this equilibrium position. Since there is no net vertical force associated with the horizontal stretching, the integration of the deflection δ over the whole ridge should be zero. Therefore the value of δ at the ridge axis should be chosen such that the summation of the vertical plastic deformation within the yield zone and the vertical elastic deflection outside the yield zone goes to zero. This requires that the near axis plastic deformation and the off axis elastic deformation be considered at the same time.

As an example, we consider a lithospheric plate which is 6 km thick at the ridge axis and thickens by 3.5 km over a distance of 15 km. Let us assume that the width of the yield zone is 15 km. The calculated vertical deflection in the yield zone is shown in Fig. 9(a) for three assumed values of $\delta(0)$. The other parameters are chosen as follows: $\mu = 0.6$, $\lambda = 0.5$, $\rho_m = 3.4 \, \text{Mg m}^{-3}$ and $\rho_w = 1.03 \, \text{Mg m}^{-3}$. As can be seen, regardless of the exact value of $\delta(0)$, the required seafloor topography should increase away from the ridge axis, forming a central valley. A $1 - 1.5 \, \text{km}$ increase in topography is necessary for yielding to occur pervasively in a plate which thickens by 3.5 km over a distance of 15 km. If this topography is present, yielding of the whole layer will occur. The required topographic slope is greater for a plate which thickens more rapidly away from the ridge axis. The greater the thickening rate, the greater the differential horizontal extensional force, and the greater the gravity sliding force required to balance the differential force. An increase in the pore fluid pressure ratio λ will decrease the strength of the plate, and decrease the required topographic slope.

The corresponding values of the depth-averaged angle between the maximum principal stress and the horizontal are plotted in Fig. 9(b). Since the plate deviates from its
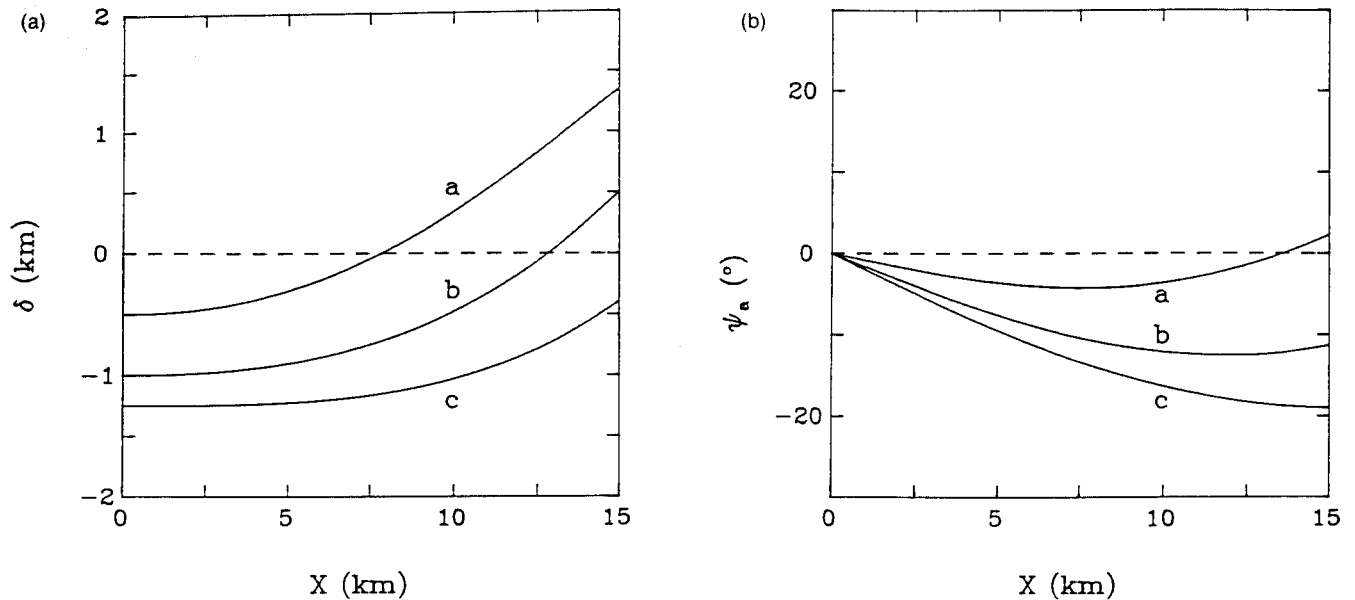
Figure 9. (a) Topographic changes required to keep a brittle plate at yield throughout. Examples are shown for three assumed values of δ at the ridge axis, $\delta(0)$. Curve a: $\delta(0) = 500$ m. Curve b: $\delta(0) = 1000$ m. Curve c: $\delta(0) = 1250$ m. To calculate the topography of a mid-ocean ridge, the value of $\delta(0)$ should be chosen such that the integration of the deformation in the plastic and elastic parts of the plate comes to zero. See text for more details. (b) $\psi_a(x)$ is the depth-averaged angle of principal stress direction. The three curves correspond to the three examples shown in (a).

isostatic equilibrium position, shear stress on vertical planes in the plate is required to balance the hydrostatic restoring force from the substratum asthenospheric fluid. This results in a rotation of principal stresses within the plate as indicated by the non-zero values of ψ_a in Fig. 9(b). The maximum value of ψ_a observed here is 20°.

Equation (16a) reveals that the force (F) required to cause a plate to yield depends primarily on the plate thickness h and the frictional coefficient μ. F increases as the square of the plate thickness; it also increases with the frictional coefficient. On the other hand, the dependence of F on ψ_a and δ is weak.

3.1.2 Significant basal stresses

Deformation in the lithosphere is related to asthenospheric flows through the stresses acting on the bottom of the lithosphere. When mantle viscosity is high, these basal stresses are significant. In fact, the basal shear stress σ_s will not only influence the force balance (equation 5a) but also affect the direction of principal stresses at bottom of the plate (equation 15b). Here we examine the importance of the basal stresses as a function of mantle viscosity.

For a prescribed athenospheric flow, basal stresses can be calculated using the boundary element method described in the last section. In a steady-state model, magmatic accretion occurs continuously at the ridge axis and the horizontal velocity of the plate is relatively uniform. To obtain a first order approximation to the basal stresses, the deviation from a constant lithospheric velocity, due to the stretching in the yield zone, is negligible. The magnitude of the basal stresses is proportional to mantle viscosity (*cf.* Phipps Morgan *et al.* 1987).

We prescribe a seafloor topography δ which increases 1.5 km over the axial yield zone (Fig. 10). We then search

for the shape h of a lithospheric plate, in which material is at yield throughout. The calculated shapes of the four plates in Fig. 10 correspond to four assumed mantle viscosities η. With the contribution from significant basal stresses (higher mantle viscosity), the same topographic slope can balance the resultant extensional force in a plate with greater thickness variation. For example, when the mantle viscosity is 5×10^{20} Pa s, the prescribed topographic change shown in Fig. 10 is sufficient to maintain the stress balance in a plate which thickens by 8 km over a distance of 15 km (the lowest curve in Fig. 10). When the mantle viscosity is less than 10^{19} Pa s, the same topographic change can only maintain the stress balance in a plate which thickens by 3.5 km over a distance of 15 km.

The solutions for mantle viscosity less than 10^{19} Pa s are indistinguishable from the solution with zero mantle viscosity (Fig. 10). This suggests that for a slow spreading mid-ocean ridge, the effect of mantle basal stresses is negligible if the mantle viscosity is less than 10^{19} Pa s. Phipps Morgan *et al.* (1987) examined the vertical stresses created by the vertical mantle flow at the base of a stretching and accreting lithosphere. Their solutions suggest that if mantle viscosity was on the order of 10^{20} Pa s, a prominent median valley would have formed at a fast-spreading ridge due to the vertical stresses created by the vertical mantle flow. Therefore, the absence of a profound median valley at fast-spreading ridges implies a mantle viscosity much smaller than 10^{20} Pa s.

3.2 Implications for the MAR axial topography

Let us examine in detail a segment of a slow-spreading ridge (MAR at 13–15 °N). Mean mirrored topography for the MAR between 13° and 15 °N (Parmentier & Forsyth 1985) is shown in Fig. 11(a) (the solid line). The full width of the
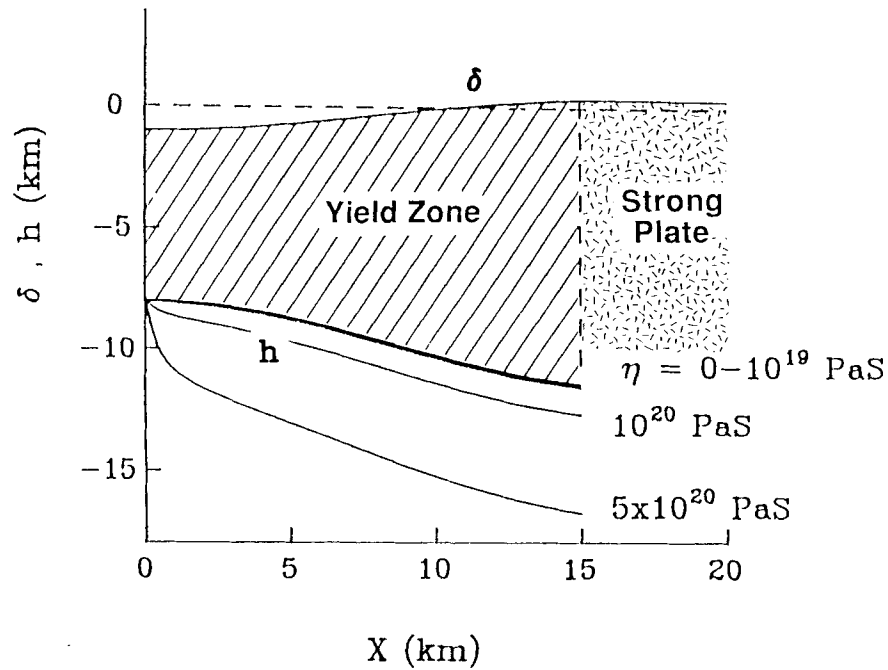
Figure 10. Seafloor topography (top solid line) required to keep various plates (bottom solid lines) at yield throughout. These plates overlie hypothetic viscous halfspaces with the shown viscosities.

median valley is about 20–30 km and the relief is over 1 km. Since we use the mean, mirrored topography as obtained by averaging individual profiles given by Collette *et al.* (1980), the variability caused by local crustal heterogeneities and being at different stages of a tectonic cycle are minimized. The free air anomaly profile over this ridge is well explained by a model in which there is no compensation for short wavelength topography but compensation of the ridge as a whole (Parmentier & Forsyth 1985).

To construct a mechanical model for the ridge, the following procedure is implemented:

(i) The thermal structure of the ridge is calculated and used to predict the lithospheric plate thickness and the thermal buoyancy force due to the temperature variation in the mantle. The effect of hydrothermal cooling is represented as an enhanced effective thermal conductivity.

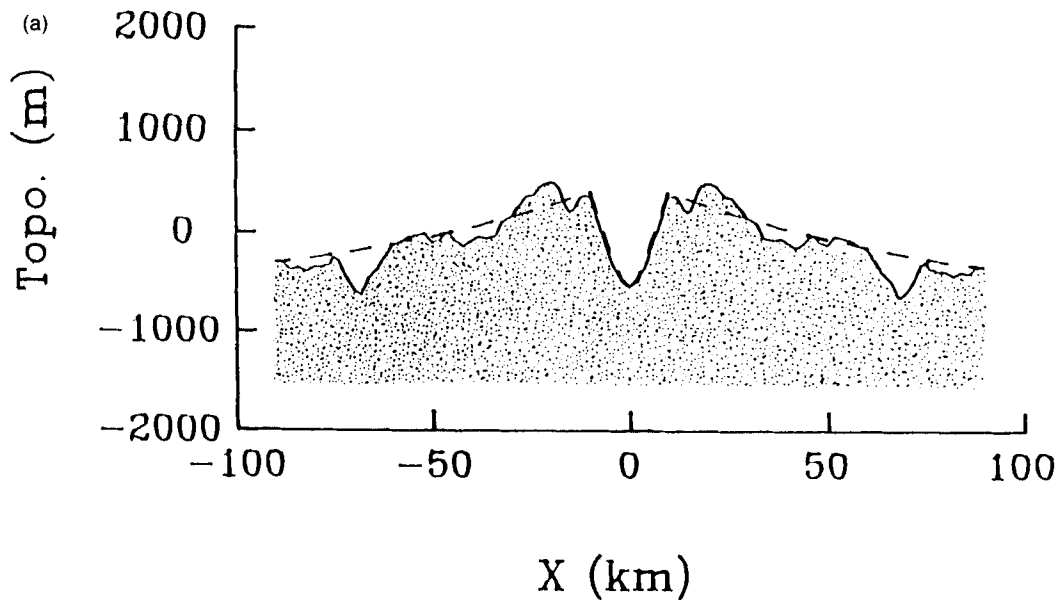(ii) The isostatic equilibrium position of the plate is

Figure 11. (a) Mean, mirrored bathymetry (the solid line) of the MAR between 13° and 15 °N (from Parmentier & Forsyth 1985). The dashed line is that predicted by a model including the thermal subsidence, the plastic necking in an axial yield zone and the elastic deflection outside the yield zone. The half width of the yield zone is 10 km. See text for details. (b) Similar to (a), except that the half width of the yield zone is 15 km.
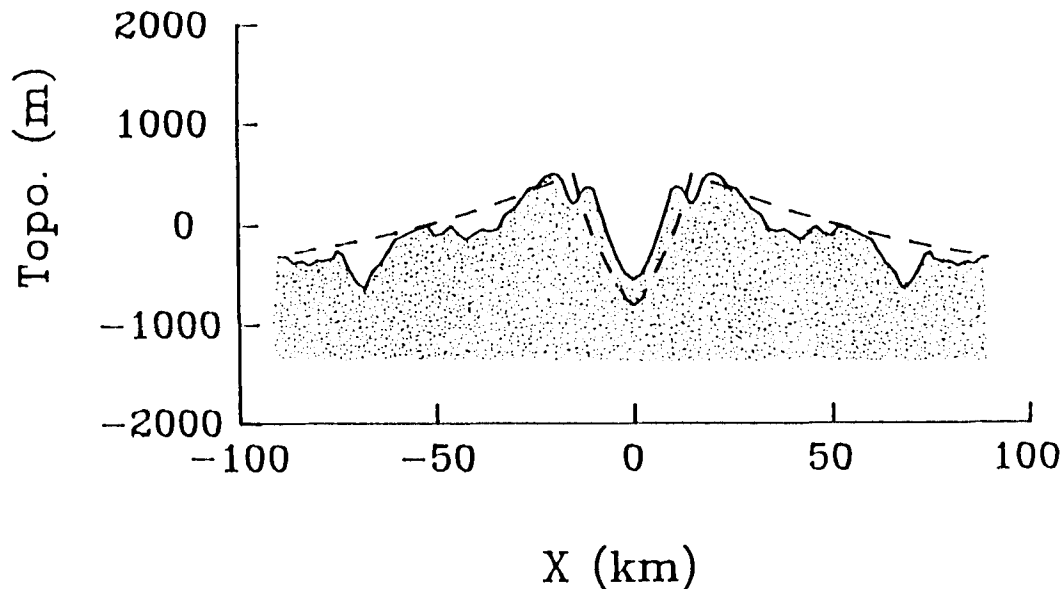
Figure 11. (*Continued*)

obtained by considering the flexure of the lithospheric plate under the thermal buoyancy force (thermal subsidence).

(iii) Assuming that the half width of the yield zone is 10 km (or 15 km), calculations are carried out to predict the topographic slope required to keep the plate at yield within 10 km (or 15 km) of the ridge axis. Outside the yield zone, the elastic deflection of the plate is obtained by requiring that the stresses and displacements be continuous at the boundary of the plastic and elastic zones. The value of the plastic deflection at the ridge axis is adjusted so that the overall integration of the vertical deformation in the plastic and elastic regions vanishes.

(iv) Theoretical topography is obtained by superimposing the plastic deflection (within the yield zone) and the elastic deflection (outside the yield zone) on the isostatic equilibrium position as predicted by the thermal model.

The predicted topography is shown by the dashed line in Fig. 11(a) and (b) for assumed yield zone widths of 10 and 15 km, respectively. The other parameters are chosen as follows: for the plastic yield zone, the frictional coefficient on the fault is $\mu = 0.6$, the fluid pressure ratio in the crust is $\lambda = 0.5$, and the mantle viscosity is 10^{19} Pa s. The lithospheric plate is assumed to be 6 km thick at the ridge axis, it thickens by 4 km over a distance of 15 km from the ridge axis. It is apparent from Fig. 11(a) that this simple model can account for the gross features of the observed bathymetry, especially that of the median valley. With other parameters kept constant, the depth of the median valley increases with the width of the valley. The inferred thickening rate of 4 km over a distance of 15 km is comparable to and slightly less than that based on the thermal models; the inferred thickening rate would be greater, however, for larger values of mantle viscosity. In the present model, the transition between the plastic and the elastic regions is assumed to take place along one vertical plane. In reality, this transition will take place through the gradual growth of an elastic core in the brittle plate.

The axial structure of mid-ocean ridges depends strongly

on spreading rate. It is, however, also influenced by factors other than the spreading rate. For example, in the vicinity of hot spots (such as the Reykjanes Ridge), an axial valley may not be present even at slow spreading rates. Due to the higher than normal magmatic heat input, these hot spot areas are characterized by a high crustal production rate. Phipps Morgan *et al.* (1987) show that the additional magmatic heat input at the ridge axis near hot spots will increase the temperature in the mantle and therefore reduce the thickness of the lithospheric plate. For example, if the crustal thickness is doubled due to the doubling in magmatic heat input at the ridge axis, the crustal and mantle temperature is greatly enhanced and the lithosphere thickness at the ridge axis is approximately halved. This could decrease the horizontal force and moment and result in a much more subtle axial rift. In contrast, the possible reduction in the magmatic heat input at the anomalously 'cold' Australian–Antarctic Discordance could result in an anomalously thicker lithosphere and deeper than normal axial topography (Forsyth, Ehrenbard & Chapin 1987).

4   INFLUENCES OF SPREADING RATE ON THE EPR TOPOGRAPHY AND GRAVITY

4.1   Observations

Based on the thermal and mechanical models we have developed in the last two sections, we will now examine the topography and gravity anomaly at the East Pacific Rise from 16° to 23 °N to detect the influence of plate spreading rate. Surface ship gravity and bathymetry profiles across three different sigments of EPR with different spreading rates were obtained from Lamont–Doherty Geological Observatory. The three regions, 16–17°, 20–21° and 22–23 °N (Fig. 12a and b), were selected for study because comparison of the bathymetry and gravity profiles between these regions allows the influence of plate spreading rate to be investigated.
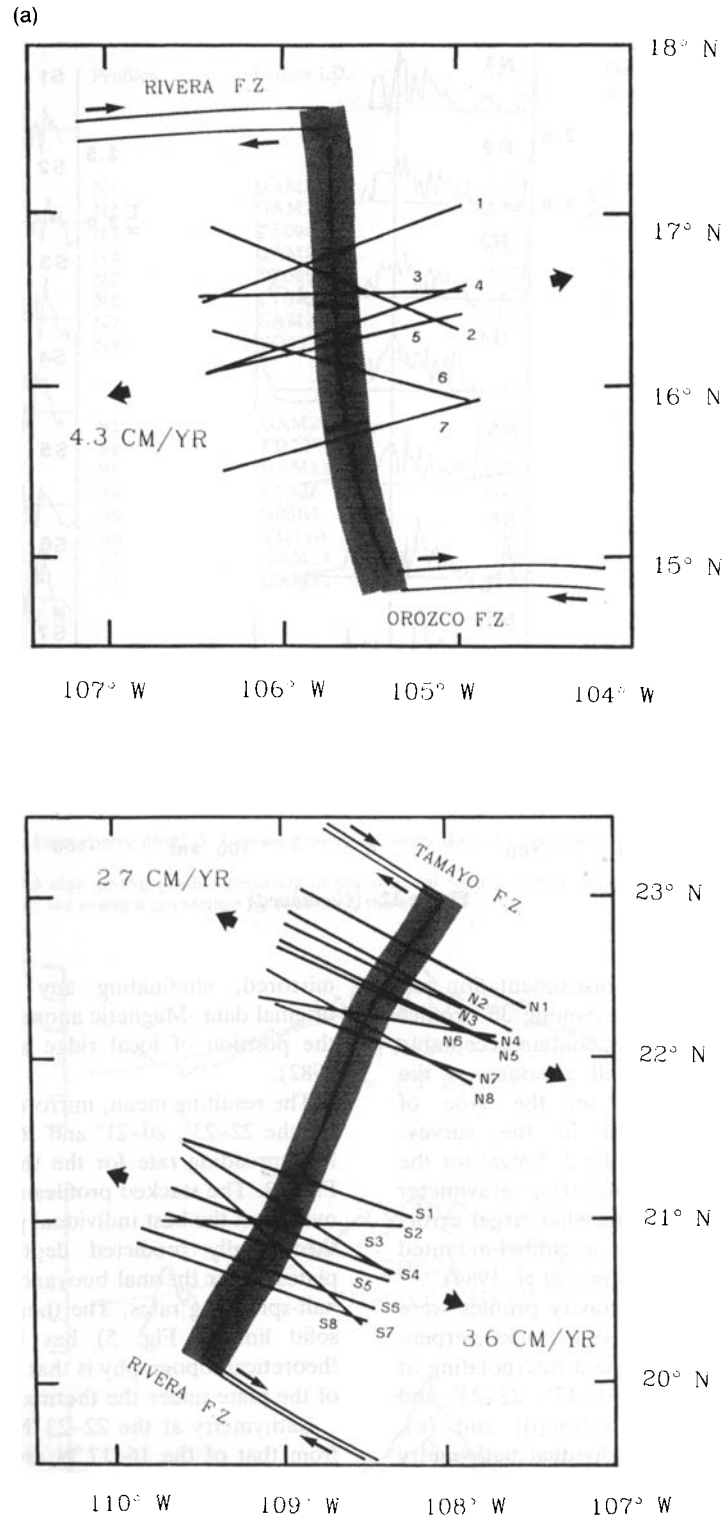
(a)

Figure 12. (a) Track line locations at the EPR at 16–17 °N. Average half-spreading rate is 4.3 cm yr^{-1}. (b) Track line locations at the EPR at 20–23 °N. The northern group (N1 to N8) locates between 22–23 °N. Average half-spreading rate is 2.7 cm yr^{-1}. The southern group (S1 to S8) locates between 20–21 °N. Average half-spreading rate is 3.6 cm yr^{-1}. (c) Individual bathymetry profiles at the EPR at 16–17 °N (d) Individual bathymetry profiles at the EPR at 22–23 °N. (e) Individual bathymetry profiles at the EPR at 20–21 °N.
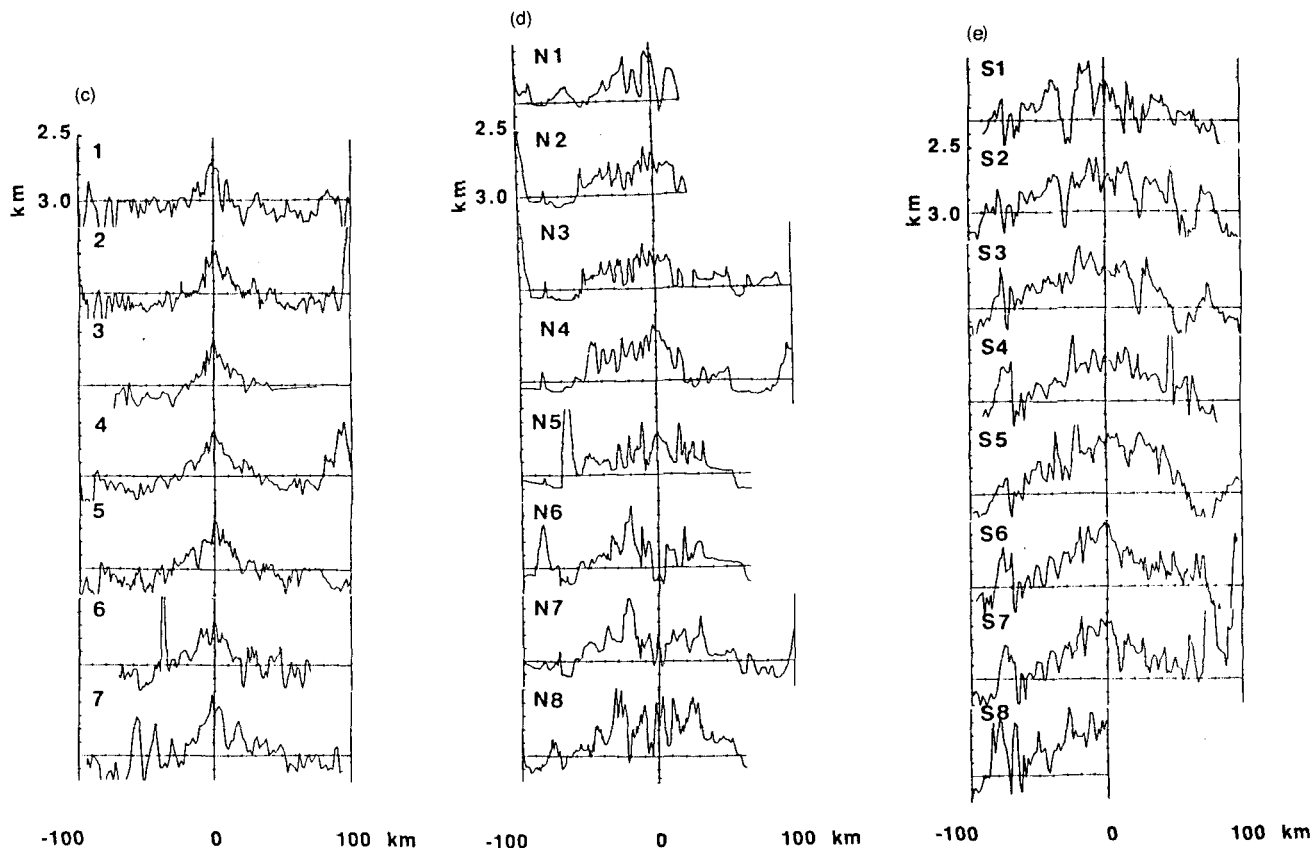
Figure 12. (*Continued*)

The data sources and information on instrumentation and navigation are summarized in Table 2. Among 30 profiles with good bathymetry, only four profiles contain acceptable gravity data (*cf.* Table 2). The overall accuracy of the gravity measurements is dependent on the type of instrumentation and navigation used in the survey. Generally, the accuracy is estimated to be 2–5 mgal for the Gss2 sea gravimeter and the vibrating-string gravimeter when used with satellite navigation. Somewhat larger errors are expected for data collected using a gimbal-mounted gravimeter and celestial navigation (Madsen *et al.* 1984).

Individual bathymetry and free air gravity profiles were constructed by projecting the original ship tracks perpendicular to the local strike of the ridge and interpolating at 2-km intervals. The profiles for the 16–17°, 22–23° and 20–21 °N areas are shown in Fig. 12(c), (d) and (e), respectively. An examination of the individual bathymetry and gravity profiles in each region reveal that although they are similar in general form, there is considerable variability from profile to profile. The fact that many of these anomalies can not be correlated between profiles strongly suggests that they are the result of local crustal heterogeneities and are not related to the fundamental structure of the ridge. In order to minimize this variability and to enhance the topographic and gravity signature associated with ridge itself, we have stacked the bathymetry and gravity data in each area. Stacking was done by summing half profiles, each 100 km long, from both sides of the rise axis. The resulting mean half profiles were than mirrored, eliminating any asymmetries present in the original data. Magnetic anomaly data was used to determine the position of local ridge axis (Klitgord & Mammerickx 1982).

The resulting mean, mirrored profiles are shown in Fig. 13 for the 22–23°, 20–21° and 16–17 °N regions. The values of half-spreading rate for the three regions are also shown in Fig. 13. The stacked profiles are a remarkable improvement over even the best individual profiles. The dashed lines show theoretically predicted depth-age relationship of elastic plates under thermal buoyancy forces for the corresponding half-spreading rates. The thermal buoyancy force $P(x)$ (the solid line in Fig. 5) has been calculated before. The theoretical topography is that predicted by the elastic flexure of the plate under the thermal buoyancy force $P(x)$.

Bathymetry at the 22–23 °N area is significantly different from that of the 16–17 °N area (Fig. 13). At the 22–23 °N area, where the plate spreads with a half-spreading rate of 2.7 cm yr^{-1} (Klitgord & Mammerickx 1982), the axial ridge topography is relatively flat and no regional axial peak exists. Within 20 km of the ridge axis, local topographic variations are small with a magnitude less than 150 m. A close examination of individual profiles reveals that topographic highs alternate with lows every 5–10 km perpendicular to the ridge axis. Such low relief topographic variation has also been found at other mid-ocean ridges with intermediate spreading rates (e.g. Juan de Fuca Ridge, Kappel & Ryan 1986).

The East Pacific Rise at 16–17°, on the other hand, shows

Table 2. Summary of data sources

	Profiles	Cruise I.D.	Year	Data Availability[1]
22-23°N				
	N1	GAM21	1968	T,M
	N2	GAM21	1968	T,M
	N3	TT099	1975	T,M
	N4	GAM21	1968	T,M
	N5	TT099	1975	T,M
	N6	TT099	1975	T,M
	N7	GAM21	1968	T,M
	N8	YQ712	1971	T
20-21°N				
	S1	GAM21	1968	T,M
	S2	FD777	1977	T,M
	S3	GAM11	1967	T,M
	S4	C1203	1968	T,G,M
	S5	SIQR1	1974	T
	S6	YQ710	1972	T,G,M
	S7	GAM11	1967	T,M
	S8	GAM11	1967	T,M
16-17°N				
	1	SCN11	1970	T,M
	2	YQ710	1972	T,M
	3	OCOCA	1969	T,M
	4	SCN11	1970	T,M
	5	YQ732	1973	T,G[2],M
	6	DPSN2	1976	T,G,M
	7	SCN11	1970	T,M

(1) T: bathymetry data; G: free-air gravity anomaly data; M: magnetic anomaly data

(2) The sign of the gravity anomaly in the original record of this cruise is obviously wrong; we made a correction by reversing the sign.
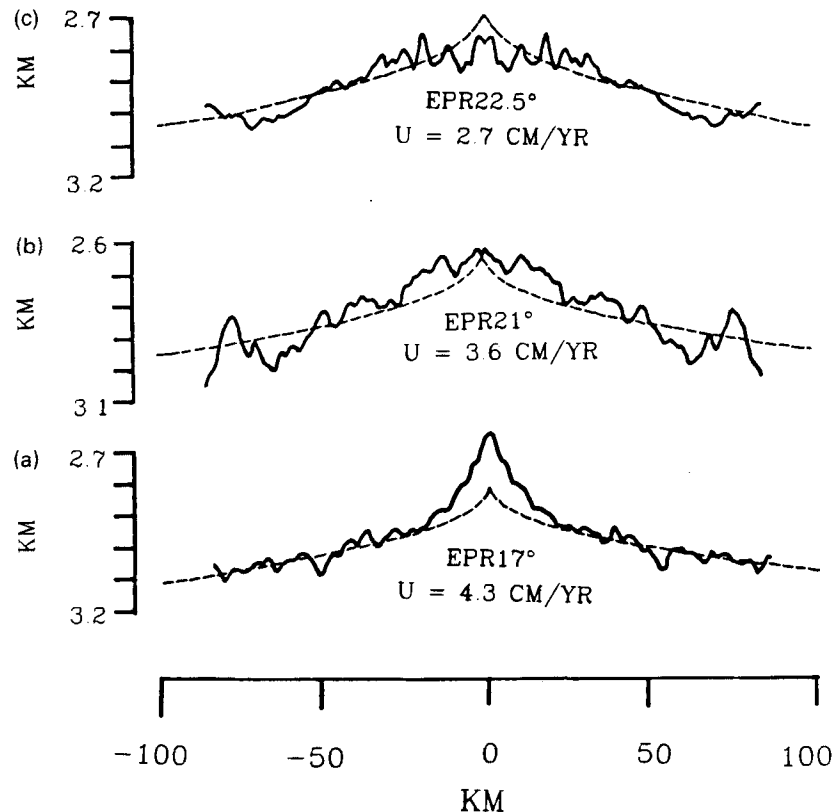

Figure 13. Mean, mirrored bathymetry for the EPR. 16–17 °N (a); 20–21 °N (b); 22–23 °N (c). The dashed lines are the computed depth-age relationship due to thermal subsidence (see text for details).
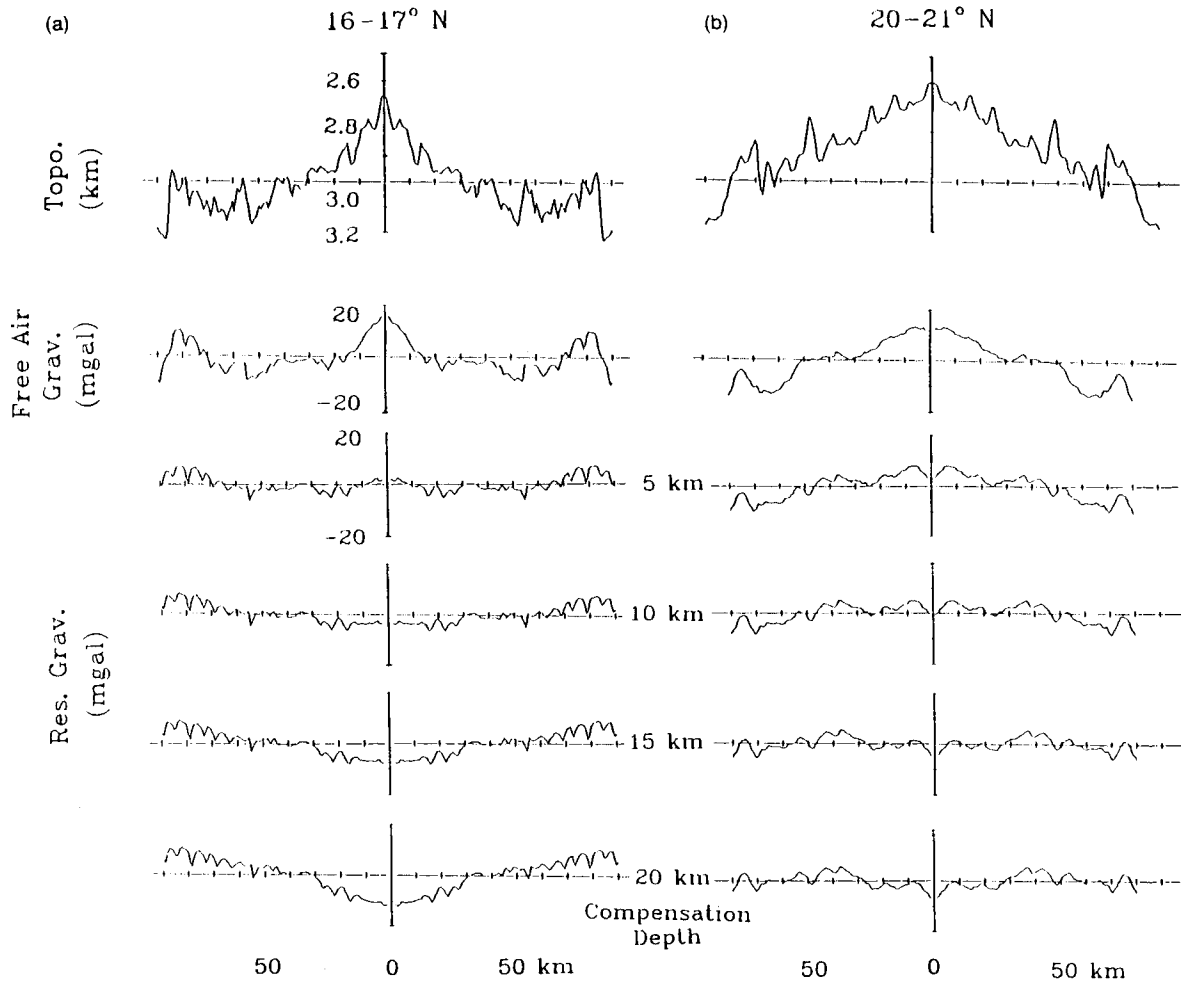
Figure 14. Residual Airy gravity anomaly for various assumed depths of compensation. (a) the EPR at 16–17 °N. (b) the EPR at 20–21 °N.

a prominent axial high with 300 m of relief over a distance of 20 km. Here the plate spreads with a half-spreading rate of 4.3 cm yr^{-1}. This topographic feature is typical of other segments of the EPR with faster spreading rates (Madsen *et al.* 1984).

Gravity anomalies give another important constraint on the thermal structure of mid-ocean ridges. The only available profiles with good gravity records are the profiles YQ732 and DPSN2 of the 16–17 °N area and C1203 and YQ710 of the 20–21 °N area (*cf.* Table 2). We will first show the compensation depth using the Airy isostasy model; a mantle Bouguer gravity anomaly will then be computed and compared with that predicted by thermal models.

To compute the calculated gravity for the Airy model, the following procedure was implemented. First, the mean, mirrored bathymetry profiles were zero meaned, cosine tapered (first and last 5 per cent), and Fourier transformed. Then, assuming a depth of compensation (Airy model), the admittance function of the isostatic model was computed and multiplied by the Fourier transform of the bathymetry. Finally, this result was inverse Fourier transformed to yield the predicted free air gravity anomaly. A density of 1.03 Mg m^{-3} was assumed for the water layer, 2.7 Mg m^{-3} for the crust, and 3.40 Mg m^{-3} for the mantle.

Residual (observed – calculated) gravity anomalies are shown in Fig. 14 for several different assumed depths of compensation. It is observed that close to the ridge the Airy compensation depth that best fits the data varies from about 7 km below the seafloor at the 16–17 °N area (Fig. 14a) to 15 km at the 20–21 °N area (Fig. 14b). These results suggest that it is unlikely that the axial topography is compensated entirely within the crust (especially at the 20–21 °N area). If this were the case, we would expect an average compensation depth of less than 5 or 6 km. Therefore, at least part of the compensation for the axial topography at the 20–21 °N area must be placed in the upper mantle below the base of the oceanic crust.

Mantle Bouguer gravity anomalies for the 16–17° and 20–21 °N areas are shown in Fig. 15(a) and (b), respectively. The mantle Bouguer anomaly is the free air anomaly corrected for the expected density effect of the displaced water/crust and crust/mantle interfaces. A crustal thickness of 6 km is assumed in the calculation. As can be seen from Fig. 15(a) and (b), in both areas the mid-ocean ridge is associated with negative mantle Bouguer gravity with an amplitude of 20 mgal over a distance of 100 km for the 16–17 °N area and 15 mgal for the 20–21 °N area. The magnitude of the negative mantle Bouguer gravity anomaly

observed here is comparable to and slightly less than that observed at other segments of the EPR with faster spreading rates (Madsen *et al.* 1984).

4.2 Tectonic implications

To examine whether the observed bathymetry and negative mantle Bouguer gravity anomaly can be explained by the density variation due to thermal expansion of mantle material, we have studied the thermal structure of the ridges with three spreading rates (similar to that in Fig. 2). A mantle temperature of 1400 °C is assumed at a depth of 100 km. Thermal diffusivity is taken to be $1 \times 10^{-6}\,\mathrm{m^2\,s^{-1}}$, and a thermal expansion coefficient of $3 \times 10^{-5}\,\mathrm{°C^{-1}}$ is assumed. A theoretical mantle Bouguer gravity anomaly is obtained by integrating the mass deficiency due to crustal and mantle temperature variations as predicted by our thermal models. The dashed lines in Fig. 15(a) and (b) show the predicted gravity anomaly. The differences between the observed and predicted mantle Bouguer (residual mantle Bouguer) gravity anomalies are plotted in Fig. 16(a) and (b) for the two ridges, respectively.

Mass deficiencies due to temperature variations in the mantle also create an integrated thermal buoyancy force $P(x)$ on the brittle lithospheric plate at a mid-ocean ridge (the solid line in Fig. 5). With an elastic plate thickness as prescribed by the 700 °C isotherm in the thermal models of Fig. 2 and with free edge boundary conditions at the ridge axis, we have calculated the flexure of the elastic plate under the buoyancy force $P(x)$. Details of the mathematical formulations and numerical techniques can be found in Kuo *et al.* (1986). The predicted topography is shown by the dashed lines in Fig. 13. The difference between the observed
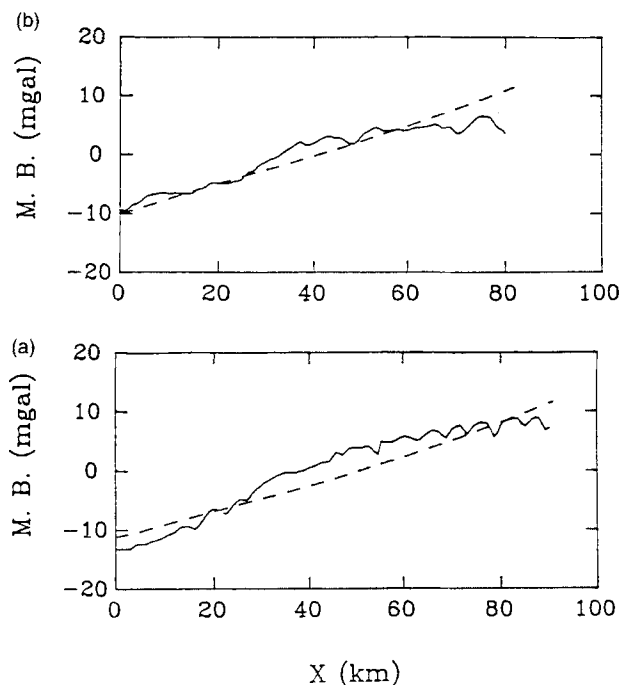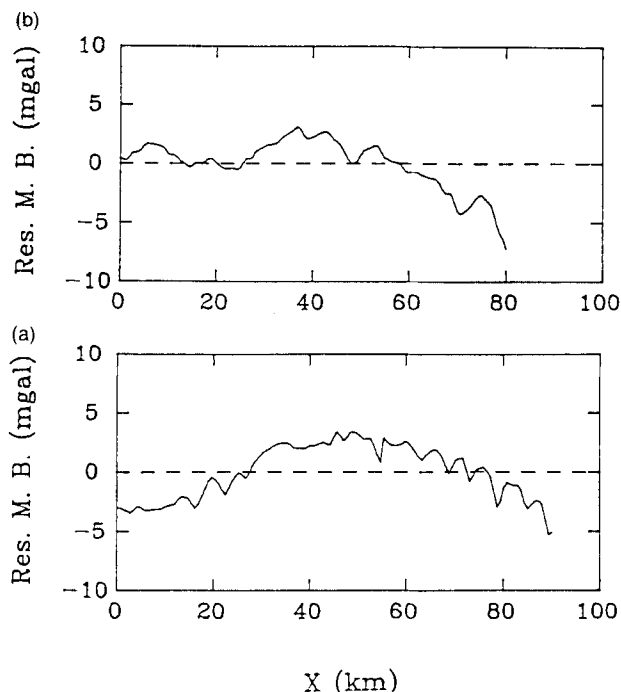

Figure 16. (a) Residual (observed-calculated) mantle Bouguer gravity anomaly at the EPR at 16–17 °N. (b) Residual (observed-calculated) mantle Bouguer gravity anomaly at the EPR at 20–21 °N.

and predicted topography (residual topography) is plotted in Fig. 17(a), (b) and (c) for the EPR at 16–17°, 20–21° and 22–23 °N, respectively.

It is apparent that mass deficiencies due to temperature variations in the mantle can account for the gross features of both the bathymetry and the mantle Bouguer gravity anomaly (Figs 13 and 15). There are, however, significant systematic local variations not explained by the model (Figs 16 and 17). For example, as the plate spreading rate decreases from 4.3 to $2.7\,\mathrm{cm\,yr^{-1}}$, the residual topography changes from an axial high to an axial low. The prominent axial high together with the negative residual gravity anomaly indicate a local concentrated low density source at the ridge axis of the 16–17 °N area. This result is similar to the findings of Madsen *et al.* (1984) and Kuo *et al.* (1986) on the structures of the EPR from 12 °N to 21 °S, where the plate spreading rate varies from 5 to $8\,\mathrm{cm\,yr^{-1}}$. According to their analysis, in addition to a broad regional low amplitude mass deficiency, a local concentrated low density body is required at the ridge axis to explain the topography and gravity. Madsen *et al.* (1984) attribute this low density body to a crustal magma chamber and a low density zone of partial melt in the upper mantle at the base of the crust.

The disappearance of the central peak at the 20–21° and 22–23 °N areas implies the following possibilities: (i) Local concentrated low density sources cease to exist at the ridge axis of the 20–21° and 22–23 °N areas. The disappearance of the negative residual gravity anomaly at the 20–21 °N area (Fig. 16b) supports this interpretation. Moreover, the long Rivera Transform Fault (Fig. 12a and b) has separated the spreading ridges at the 16–17° and 20–23 °N areas and two

Figure 15. (a) Observed mantle Bouguer gravity anomaly (the solid line) at the EPR at 16–17 °N. Theoretically predicted gravity anomaly is shown by the dashed line. (b) Observed (the solid line) and predicted (the dashed line) gravity at the EPR at 20–21 °N.
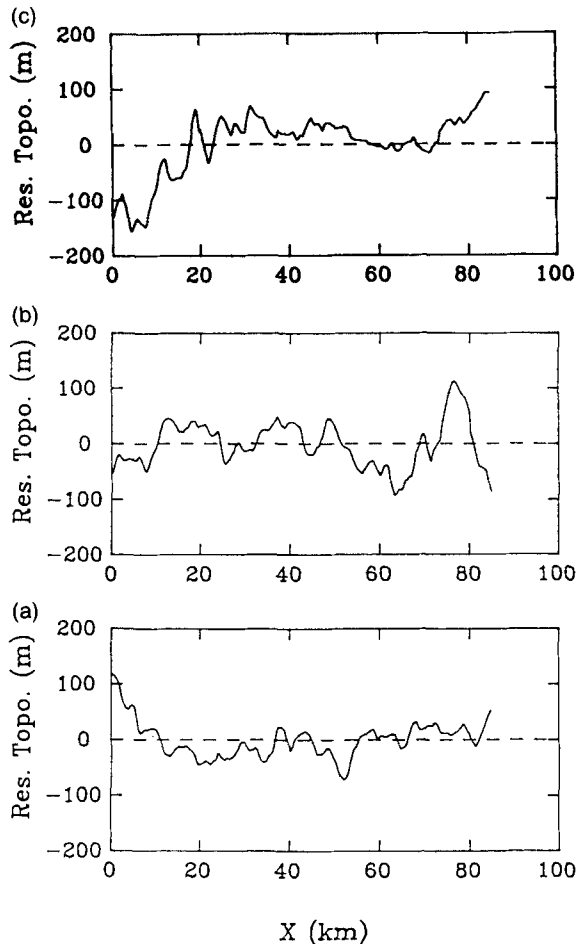
ridge segments may operate independently. (ii) The 2.7 cm yr^{-1} half-spreading rate at the 22–23 °N area is slow enough that an axial valley which is characteristic of a slow spreading ridge starts to form (Fig. 17c). The large width of the axial topographic low (15–20 km of half-width) suggests that it is of tectonic and not magmatic origin. The 200 m axial low observed here is, however, much less than the 1–2 km observed at the very slow-spreading ridges (e.g. the MAR, Macdonald & Luyendyk 1977).

To explain this residual topography, similar calculations have been carried out for the 22–23 °N area. The mean, mirrored topography is shown by the solid line in Fig. 18. The dashed line is the topography required to keep the central 20 km (half width) of the brittle plate at yield. Our analysis reveals that if the basal stresses from the asthenospheric flow are negligible, the observed 200 m topographic relief at the 22–23 °N area is sufficient only to cause some yielding throughout the plate, which thickens by 0.7 km over a distance of 20 km from the ridge axis. With the addition of basal stresses, the corresponding changes in plate thickness can be greater. If pervasive failure does occur in an axial zone at the 22–23 °N area, the observed small residual topography indicates that the lithospheric plate at the EPR at 22–23 °N thickens much more slowly than that of the MAR.

5 CONCLUSIONS

Gravity and bathymetry of the East Pacific Rise (EPR) from 16 °N (half-spreading rate 4.3 cm yr^{-1}) to 23 °N (half-spreading rate 2.7 cm yr^{-1}) show systematic variations with plate spreading rate. On a regional scale, the observed topography can be explained by the flexure of an elastic plate under the thermal buoyancy due to temperature variations in the mantle (thermal subsidence). The observed regional gravity anomaly can also be explained by mantle temperature variations. A systematic deviation from the regional compensation is, however, observed at the ridge

Figure 17. (a) Residual (observed-calculated) topography at the EPR at 16–17 °N. (b) Residual (observed-calculated) topography at the EPR at 20–21 °N. (c) Residual (observed-calculated) topography at the EPR at 22–23 °N.
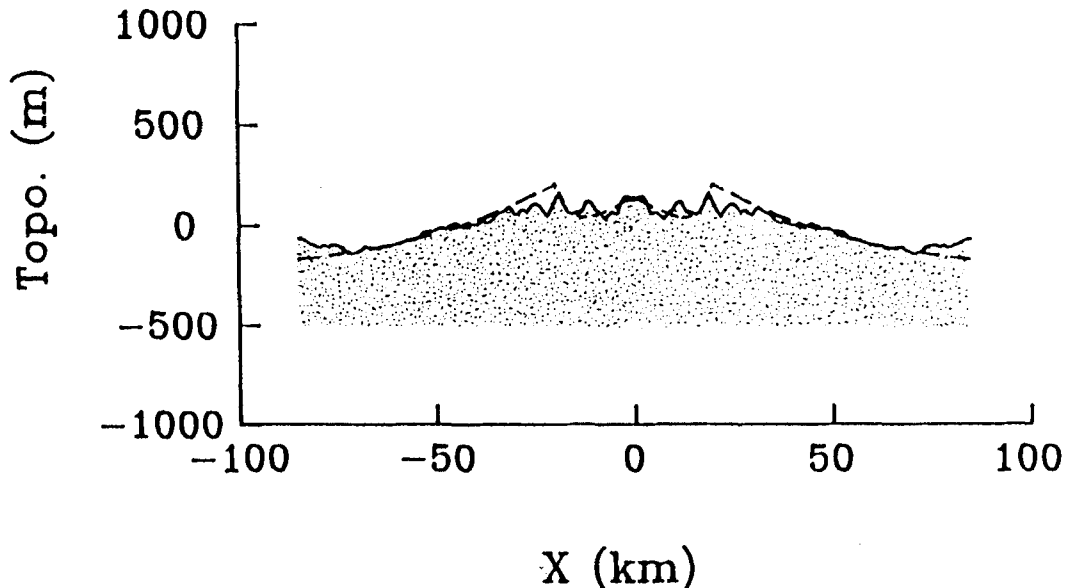

Figure 18. Mean, mirrored bathymetry (the solid line) of the EPR between 22° and 23 °N. The dashed line is the topography required to maintain the throughout yielding in a plate whose thickness increases by 0.7 km over a distance of 20 km. See text for details.

axis. Prominent residual local topographic high and gravity low are observed at the ridge axis of the EPR 16–17 °N, where the plate spreads at a relatively fast rate. This residual axial high gradually disappears to the north as the plate spreading rate decreases; at the EPR 22–23 °N a residual low at ridge axis is observed instead. We propose that a low density body exists at the ridge axis of the EPR 16–17 °N, causing the observed axial topographic high and residual gravity low. Such a low density body is, however, not required for the ridge north of the EPR 20 °N. The observed axial topographic low at the EPR 22–23 °N is likely related to the extension of the brittle plate in an axial yield zone. The topography caused by the extension becomes significant at the EPR 22–23 °N because the plate spreads more slowly and thickens more rapidly away from ridge axis.

Thermal models of a mid-ocean ridge are developed which include the effects of lithospheric thickening on the mantle flow, the heat of magmatic crustal accretion at the ridge axis, and the hydrothermal cooling due to seawater circulation in the crust. For a typical slow spreading ridge, several kilometres of plate thickening are expected within a distance of 15 km. When subject to extensional force, shear failure by faulting will occur in a yield zone at the ridge axis. Approximate solutions for the stress distribution in an elastic-perfectly plastic plate are obtained. To keep the plate at yield in the axial yield zone, a significant increase in the seafloor topography away from the ridge axis is required. Basal stresses from the viscously deforming asthenosphere can affect lithospheric stresses only if the mantle viscosity is on the order of 10^{20} Pa s, significantly higher than generally accepted values of 10^{18} Pa s. The horizontal extensional force required to cause a plate to yield is proportional to the square of the plate thickness.

Model studies are carried out to analyse the stretching of the lithospheric plates at the MAR 13–15 °N and the EPR 22–23 °N. It is shown that at the MAR 13–15 °N, the deviation of the lithospheric plate from the isostatic equilibrium position can be well explained by stretching due to faulting in an axial yield zone and elastic deflection outside the yield zone. The half width of the yield zone is 10–15 km. If pervasive failure also occurs at the axial zone at the EPR 22–23 °N, the small residual topography implies that the lithospheric plate at the EPR 22–23 °N thickens much more slowly than that at the MAR.

ACKNOWLEDGMENTS

REFERENCES

Atwater, T. M., 1979. Constraints from the Famous area concerning the structure of the oceanic section, in *Deep Drilling Results in the Atlantic Ocean: Ocean Crust*, pp. 33–42,

eds Talwani, M., Harrison, C. G. & Hayes, D. E., 2, American Geophysical Union, Washington, DC.

Bergman, E. A. & Solomon, S. C., 1984. Source mechanisms of earthquakes near mid-ocean ridges from body waveform inversion: Implications for the early evolution of oceanic lithosphere, *J. geophys. Res.*, **89**, 11415–11441.

Brace, W. F. & Kolstedt, D. L., 1980. Limits on lithosphere stress imposed by laboratory experiments, *J. geophys. Res.*, **85**, 6248–6252.

Bicknell, J. D., Sempere, J.-C., Macdonald, K. C. & Fox, P. J., 1987. Tectonics of a fast spreading center: A deep-tow and Seabeam survey at EPR 19°30'S, *Mar. geophys. Res.*, **8**, 131–148.

Bryan, W. B. & Moore, J. G., 1977. Compositional variations of young basalts in the Mid-Atlantic ridge rift valley near lat. 36°49'N, *Bull. geol Soc. Am.*, **88**, 556–570.

Cochran, R. R., 1979. An analysis of isostasy in the world's oceans, 2. Midocean ridge crests, *J. geophys. Res.*, **84**, 4713–4729.

Chapple, W. M., 1978. Mechanics of thin-skinned fold-and thrust belts, *Bull. geol. Soc. Am.*, **89**, 1189–1198.

Collette, B. J., Verhoef, J. & de Mulder, A. F. J., 1980. Gravity and a model of the median valley, *J. Geophys.*, **47**, 91–98.

Crane, K. & Ballard, R. D., 1981. Volcanics and structure of the FAMOUS Narrowgate rift: evidence for cyclic evolution, *J. geophys. Res.*, **86**, 5112–5124.

Crouch, S. L. & Starfield, A. M., 1983. *Boundary Element Methods in Solid Mechanics*, Allen and Unwin, Boston.

Dahlen, F. A., Suppe, J. & Davis, D., 1984. Mechanics of fold-and thrust belts and accretionary wedges: Cohesive Coulomb theory, *J. geophys. Res.*, **89**, 10087–10101.

Davis, D., Suppe, J. & Dahlen, F. A., 1983. Mechanics of fold-and thrust belts and accretionary widges, *J. geophys. Res.*, **88**, 1153–1172.

Detrick, R. S., Buhl, P., Vera, E., Mutter, J., Orcutt, J., Madsen, J. & Brocher, T., 1987. Multi-channel seismic imaging of a crustal magma chamber along the East Pacific Rise, *Nature*, **326**, 35–41.

Detrick, R. S., Fox, P. J., Schulz, N., Pockalny, R., Kong, L., Mayer, L. & Ryan, W. B. F., 1988. Geological and tectonic setting of the MARK area, *Proc. Ocean Drill. Prog.*, 106/109, Part A, Initial Reports, College Station, TX (Ocean Drilling Program).

Forsyth, D. W., Ehrenbard, R. L. & Chapin, S., 1987. Anomalous upper mantle beneath the Australian–Antarctic Discordance, *Earth planet. Sci. Lett.*, **84**, 471–478.

Hill, R., 1950, *The Mathematical Theory of Plasticity*, Oxford University Press.

Huang, P. Y. & Solomon, S. C., 1987. Centroid depths and mechanisms of Mid-Atlantic Ridge earthquakes in the Indian Ocean, Gulf of Aden, and Red Sea, *J. geophys. Res.*, **92**, 1361–1382.

Huang, P. Y., Solomon, S. C., Bergman, E. A. & Nabelek, J. L., 1986. Focal depths and mechanisms of Mid-Atlantic Ridge earthquakes from body waveform inversion, *J. geophys. Res.*, **91**, 3724–3738.

Hyndman, R. D. & Rankin, S. J., 1972. The Mid-Atlantic Ridge near 45°N XVII. Heat flow measurements, *Can. J. Earth Sci.*, **9**, 664–670.

Jemsek, J. P., Bergman, E. A., Nabelek, J. L. & Solomon, S., 1986. Focal depths and mechanisms of large earthquakes on the Arctic mid-ocean ridge system, *J. geophys. Res.*, **91**, 13993–14005.

Kappel, E. S. & Ryan, W. B. F., 1986. Volcanic episodicity and non-steady-state rift valley along Northeast Pacific Spreading Centers: Evidence from Sea MARC I, *J. geophys. Res.*, **91**, 13925–13940.

Karson, J. A., Thompson, G., Humphris, S. E., Edmond, J. M., Byran, W. B., Brown, J. R., Winters, A. T., Pockalny, R. A., Casey, J. F., Campbell, A. C., Klinkhammer, G., Palmer, M. R., Kinzler, R. J. & Sulanowska, M. M., 1987. Along-axis variations in seafloor spreading in the MARK area, *Nature*, **328**, 681–685.

Klitgord, K. D. & Mammerickx, J., 1982. Northern East Pacific Rise: Magnetic anomaly and bathymetric framework, *J. geophys. Res.*, **87**, 6725–6750.

Kuo, B. Y., Forsyth, D. W. & Parmentier, E. M., 1986. Flexure and thickening of the lithosphere at the East Pacific Rise, *Geophys. Res. Lett.*, **13**, 681–684.

Kuznir, N. J., 1980. Thermal evolution of the oceanic crust; its dependence on spreading rate and effect on crustal structure, *Geophys. J. R. astr. Soc.*, **61**, 167–181.

Lachenbruch, A. H., 1973. A simple mechanical model for oceanic spreading centers, *J. geophys. Res.*, **78**, 3395–3417.

Lachenbruch, A. H., 1976. Dynamics of a passive spreading center, *J. geophys. Res.*, **81**, 1883–1902.

Laughton, A. S. & Searle, R. C., 1979. Tectonic processes on slow spreading ridges, in *Deep Drilling Results in the Atlantic Ocean: Ocean Crust*, pp. 15–32, eds Talwani, M., Harrison, C. G. & Hayes, D. E., 2, American Geophysical Union, Washington, DC.

Le Pichon, X. & Langseth, M. G., 1969. Heat flow from the mid-ocean ridges and sea floor spreading, *Tectonophys.*, **8**, 319–344.

Lewis, B. T. R., 1981. Constrains on the structure of the East Pacific Rise from gravity, *J. geophys. Res.*, **87**, 8491–8500.

Lewis, B. T. R., 1982. Isostacy, magma chambers, and plate driving forces on the East Pacific Rise, *J. geophys. Res.*, **86**, 4868–4880.

Lin, J. & Parmentier, E. M., 1987. Mechanisms of lithosphere extension at mid-ocean ridges, *Eos, Trans. Am. geophys. Un.*, **68**, 407.

Lister, C. R. B., 1983. On the intermittency and crystallisation mechanisms of sub-seafloor magma chambers, *Geophys. J. R. astr. Soc.*, **73**, 351–366.

Lonsdale, P., 1977. Structural geomorphology of a fast-spreading rise crest: The East Pacific Rise near 3°25'S, *Mar. geophys. Res.*, **3**, 251–293.

Macdonald, K. C., 1977. Near bottom magnetic anomalies, asymmetric spreading, and tectonics of the Mid-Atlantic Ridge near lat 37°N, *Bull. geol. Soc. Am.*, **88**, 541–555.

Macdonald, K. C. & Luyendyk, B. P., 1977. Deep-tow studies of the Mid-Atlantic Ridge crest near lat 37°N, *Bull. geol. Soc. Am.*, **88**, 621–636.

Madsen, J. A., Forsyth, D. W. & Detrick, R. S., 1984. A new isostatic model for the East Pacific Rise crest, *J. geophys. Res.*, **89**, 9997–10015.

Morton, J. L. & Sleep, N. H., 1985. A mid-ocean ridge thermal model: Constraints on the volume of axial hydrothermal heat flux, *J. geophys. Res.*, **90**, 11345–11353.

Ocean Drilling Program Leg 106 Scientific Party, 1986. Drilling the Snake Pit hydrothermal sulfide deposit on the Mid-Atlantic Ridge, lat 22°22'N, *Geology*, **14**, 1004–1007.

Parmentier, E. M. & Forsyth, D. W., 1985. Three-dimensional flow beneath a slow spreading ridge axis: a dynamic contribution to deeping of the median valley toward fracture zones, *J. geophys. Res.*, **90**, 678–684.

Phipps Morgan, J., Parmentier E. M. & Lin, J., 1987. Mechanisms for the origin of mid-ocean ridge axial topography: Implications for the thermal and mechanical structure of accreting plate boundaries, *J. geophys. Res.*, **92**, 12823–12836.

Reid, I. & Jackson, H. R., 1981. Oceanic spreading rate and crustal thickness, *Marine geophys. Res.*, **5**, 165–172.

Rona, P., 1985. Black smokers and massive sulfides at the TAG hydrothermal field, Mid-Atlantic Ridge, 26 °N, *Eos, Trans. Am. geophys. Un.*, **66**, 936.

Schouten, H. & Denham, C. R., 1979. Modeling the oceanic magnetic source layer, in *Deep Drilling Results in the Atlantic Ocean: Ocean Crust*, pp. 151–159, eds Talwani, M., Harrison, C. G. & Hayes, D. E., 2, American Geophysical Union, Washington, DC.

Sclater, J. G. & Francheteau, J., 1970. The implications of terrestrial heat flow observations on current tectonic and geochemical models of crust and upper mantle of the earth, *Geophys. J. R. astr. Soc.*, **20**, 509–542.

Searle, R., 1984. Gloria survey of the East Pacific Rise near 3.5 °S: Tectonic and volcanic characteristics of a fast spreading mid-ocean rise, *Tectonophys.*, **101**, 319–344.

Sleep, N. H., 1969. Sensitivity of heat flow and gravity to the mechanism of sea-floor spreading, *J. geophys. Res.*, **74**, 542–549.

Sleep, N. H., 1975. Formation of the oceanic crust: some thermal constraints, *J. geophys. Res.*, **80**, 4037–4042.

Sleep, N. H. & Rosendahl, B. R., 1979. Topography and tectonics of mid-oceanic ridge axes, *J. geophys. Res.*, **84**, 6831–6839.

Spiess, F. N., Macdonald, K. C., Atwater, T., Ballard, R., Carranza, A., Cordoba, D., Cox, C., Diaz Gracis, V. M., Francheteau, J., Guerrero, J., Hawkins, J., Haymon, R., Hessler, R., Juteau, T., Kastner, M., Larson, R., Luyendyk, B., MacDougal, J. D., Miller, S., Normark, W., Orcutt, J. & Rangin, C., 1980. East Pacific Rise: hot springs and geophysical experiments, *Science*, **207**, 1421–1433.

Stakes, D. S., Shervais, J. W. & Hopson, C. A., 1984. The volcanic-tectonic cycle of the FAMOUS and MAR valleys, Mid-Atlantic Ridge (36°47'N): Evidence from basalt glass and phenocryst compositional variations for a steady-state magma chamber beneath the valley midsections, AMAR 3, *J. geophys. Res.*, **89**, 6995–7028.

Talwani, M., Windish, C. C. & Langseth, M. G., Jr., 1971. Reykjanes Ridge crest: a detailed geophysical study, *J. geophys. Res.*, **76**, 473–517.

Tapponier, P. & Francheteau, J., 1978. Necking of the lithosphere and the mechanics of slowly accreting plate boundaries, *J. geophys. Res.*, **83**, 3955–3970.

Timoshenko, S. & Wornowsky-Krieger, S., 1959. *Theory of Plates and Shells*, McGraw-Hill, New York.

Toomey, D. R., Solomon, S. C., Purdy, G. M. & Murray, M. H., 1985. Microearthquakes beneath the median valley of the Mid-Atlantic Ridge near 23 °N: Hypocenters and focal mechanisms, *J. geophys. Res.*, **90**, 5443–5458.

Wiens, D. A. & Stein, S., 1984. Intraplate seismicity and stresses in young ocenaic lithosphere, *J. geophys. Res.*, **89**, 11442–11464.

Wolery, T. J. & Sleep, N., 1976. Hydrothermal circulation and geochemical flux at mid-ocean ridges, *J. Geol.*, **84**, 249–275.